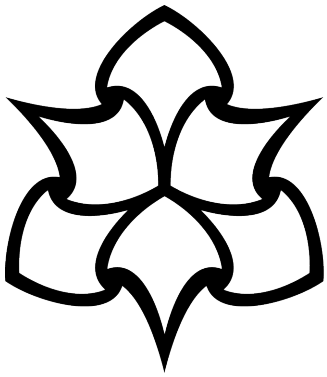

Studies of Wear and Tear and Hydrogen Bonding in Dendrimeric Fluorinated Polysilsequioxanes Coatings on an Aluminum Surface

Atul Tiwari[1,2], Tomasz W Liskiewicz[3], Lloyd Hihara[2]

[1-] Pantheon Chemical Inc., Phoenix, 85027, AZ, USA.

[2]-Department of Mechanical Engineering, University of Hawaii at Manoa, Honolulu, 96822, USA.

[3]- School of Mechanical Engineering, University of Leeds, Leeds LS2 9JT, UK.

ABSTRACT

This paper explores the physicochemical and physicomechanical process occurring during the formation of dendrimeric fluorinated polysilsesquioxanes (PSSQ) coated over active aluminium surface. The changes in chemical composition of PSSQ have been monitored as a function of time and investigated using FTIR 2D correlation spectroscopy. The percolation of water molecules, hydrogen bonding and interference of several physicochemical processes occurring in curing and crosslinking reaction in PSSQ have been monitored. The changes in surface morphology as a function of time have been recorded with atomic force microscopy and correlated with the nanomechanical analyses through nanoindentation. Specifically, nanoscratch and wear resistance was recorded at various time intervals to understand the transformation in the surface characteristics of the material. The ultimate aim of this work was to understand the correlation between reacting ingredients, surface features, wear and friction by applying a self-lubricated coating made of fluorinated PSSQ over an aluminium surface. Attempts have been made to understand how the quantity and interaction of water molecules control the hydrolysis, condensation and subsequent crosslinking reactions. The degree of crosslinking eventually controls the hardness and adhesion characteristics of the molecules, which in turn control the

surface topology, resulting friction, wear resistance and, consequently, surface life span of the material.

Keywords: Hydrogen bonding, Energy analysis, Wear, Friction, Polysilsesquioxanes, Morphology

1. INTRODUCTION

Excessive wear is caused by friction between sliding bodies and friction tends to increase with progressive wear on a surface. An adequate amount of friction is required for motion. Wear and friction have been thoroughly investigated over the past few decades [1-5]. A keyword search "Wear Analysis" resulted in 41,000 articles and, of these, more than 21,000 articles (Figure 1a) appeared in the past 10 years (between 2006 and 2015). This means that, on a global scale, more than 2,000 articles were published every year on this subject in the past decade. The majority of these articles are contributed by the materials science and engineering fraternity. As mentioned recently by James and Robert [6], an enormous amount of money is wasted due to the inadvertent failure of vehicles, machines and devices due to wear. It is worth mentioning that this subject has been extensively discussed in conferences (Figure 1b). Although this field is being vigorously researched, our understanding on the subject is still limited and new information brings new surprises. Historically, the limitation on the resolution limit of available instruments posed a big hurdle in developing an in-depth understanding of the wear-mediated failures of surfaces. However, new techniques such as atomic force microscopy have helped researchers to record minute details of wearing surfaces that were unavailable earlier [7-8]. Similarly, instrumented nanoindentation has been extensively utilized in investigation of nanomechanical analysis of surfaces [9]. Nanoindentation provides the user with complete control over mechanical analysis not available with any other technique. Surface analysis using nanoindentation is deemed to have

provided a breakthrough in our understanding of wear. The selection of appropriate film or coating material, metal surface and carefully designed experimentation are critical in drawing meaningful results from such analysis.

A few scattered investigations have highlighted the development of self-lubricating films or coatings providing favourable surface characteristics that may impart long-lasting wear resistance to metals and quasi-metals. It is also noticed that molecular engineered PSSQ have been widely studied as coating material and can be tuned to develop self-lubricating film [10-11]. PSSQ are considered hybrid composites that have characteristics of both organic and inorganic components [12-13]. PSSQ can be synthesized adopting sol-gel polymerization via hydrolysis and subsequent condensation of functional silanes [14]. The polymerization and crosslinking reaction leading to a 3D network could be facilitated either through heating or using a catalyst. The ultimate SiOSi backbone structure could be tailored by adopting suitable polymerization and processing conditions [15-16]. The chemical and physical properties of such quasi-ceramic materials are mostly the function of covalently attached domains of organic and inorganic moieties [17]. The physical properties of such materials can, however, be tuned by controlling the domain sizes. A significant improvement in physical properties is often achieved by reducing the respective domain sizes, thereby increasing the surface area. It is, therefore, sufficient to mention that domain sizes of organic and inorganic entities in the hybrid material play a pivotal role in controlling the morphology and properties of the ultimate material [18-19].

The silsesquioxanes are most commonly represented by the empirical formula $RSiO_{1.5}$ (where R could be a hydrogen or alkyl group) which can be prepared with varying domain sizes by merely changing the length of alkyl chains attached to the organic/inorganic counterparts [20]. Densely packed PSSQ are obtained by reacting bi- or tri-functional silyl groups containing smaller alkyl

chains with non-hydrolysable carbon silicon bond [21-22]. Such PSSQ contain coexisting organic domains distributed homogenously without phase separation. While the use of larger alkyl chain length could result in semi-porous morphology, the use of smaller organic linkages could lead to a greater degree of control over the final pores and distribution [23].

The degree of hydrolysis of alkoxysilanes is affected by the presence of an alkyl side chain as well as the presence of an acidic or alkaline catalyst. Brinker [24] mentioned that a condensation reaction producing alcohol is favoured when water less than a stoichiometric amount is used, while water forming condensation is favoured when a large amount of water is used. However, the presence of a greater amount of water often promotes the depolymerizaion via reverse hydrolysis. The use of an adequate amount of water for the hydrolysis has been advocated by numerous researchers [25-26]. When using less water than a stoichiometric amount, the complete hydrolysis of labile group is prevented due to several competing reactions including the formation of hydrogen bonding with hetero atoms. The volume of diffusing water molecules during the ambient condition for curing of PSSQ would be critical under such circumstances.

The information on the amount of water available for the hydrolysis of silanes and subsequent condensation has been studied by several spectroscopic techniques, such as FTIR [27-29], Raman [30-31], UV-vis, NMR [32], neutron scattering, etc. [33-34]. Among various spectroscopic techniques, the 2D COS FTIR analysis has gained significant attention [35]. This technique, originally proposed by Noda, has been widely accepted for the elucidation of the chemical phenomenon occurring in materials as a function of external perturbation [36-37]. 2D COS is extremely valuable in understanding the chemistry of the system with functional groups containing bonds that overlap with those for intermolecular or intramolecular hydrogen bonded water molecules [38]. The presence of O-H band originating from various chemical entities may appear in a broad spectral

regime depending on the neighbouring atoms. For example, O-H band from hydrogen bonded water is analysed in the region between 3,200 and 3,800 cm^{-1} [39], while, in fingerprint region, the O-H bond appears between 940 and 980 cm^{-1} in silanol, between 910 and 930 cm^{-1} in epoxy and between 870 and 950 cm^{-1} in pure alcohols. Mizuse et al. [28, 40] in a series of articles demonstrated that O-H bond vibration frequency, intensity, peak shape and position vary as a function of water molecule clustering and the nature of the hydrogen bond existing with or between the clusters. The availability of free water molecules to hydrolyse alkoxysilane will, therefore, enumerate the condensation of silanols. As Suresh [41] mentioned, the surface morphological features are primarily responsible for the resultant nanomechanical properties of materials. In our present study, the authors will also point out that properties are pivoted to the amount of silanol condensation as a function of time.

An analysis of the literature leads to the finding that, upon the application of silicone as a coating/film material, these are hydrolysed on exposure to moist air and labile group significantly interfere with reaction proceedings. In ambient conditions, the catalyst assists in condensation of silanols with the release of facilitator water molecules. The top layer primarily densifies while the underlying layers are still waiting for the in-diffusion of water molecules. In such case, the hydrolysis and condensation reaction will gradually slow down and eventually stop due to the non-replenishing water molecules. The gradual development of residual stress in succeeding layers and retarded out-diffusing volatile organic molecules will generate micropores or cracks on the surface. The question of how much water is adequate to successfully carry out the hydrolysis reaction in the bulk of solution without affecting the condensation has intrigued scientists for many years. Moreover, how the flooding or drought of water molecules around the labile groups would eventually govern the topological features or nanostructures on the surface is

not well understood. Additionally, the way in which the presence of structural features contributes to the friction and overall wear resistance of material is still mystifying.

The strength of high-performance materials at nanoscopic domain can be evaluated with the automated nanoindentation technique (ANT) [42]. The ANT has been widely utilized to measure the response of materials on application of load. While typical tests include elastic, plastic, elasto-plasticity, cracking or fracture, special test methods can conduct wear deformation on materials similar to that in the rolling ball method. Studies, however, have not been reported on the systematic nanoscopic wear analysis of coatings using ANT. The experimentation in this article will attempt to trace the path of water molecules during the adsorption, hydrolysis, condensation and subsequent effect on crosslinking reactions in material, which in turn affect the surface morphology and wearing characteristics of the material.

2. MATERIALS AND METHODS

2.1 Development of the PSSQ

The chemicals that were procured for the synthesis of PSSQ precursor are as follows: methyltrimethoxysilane (purity 98%), methyltriacetoxysilane (purity 95%), tetramethoxysilane (purity 97%) and (3,3,3-trifluropropyl) methyldimethoxysilane purchased from Gelest; dibutyltindilaurate catalyst (purity 95%) purchased from Alfa Aesar; isopropanol (ACS grade) purchased from Sigma Aldrich, USA; and sodium bicarbonate purchased from Merck. Titanium ethoxide was purchased from Alfa Aesar. All of the chemicals were analytical grade as quoted by the manufacturer and used without further purification and recrystallization. Ultrapure water of 18 MΩ•cm resistivity was used in this study.

A modified green quasi-ceramic PSSQ precursor was prepared by following the patented procedure briefly described as follows [43-44]: A mixture of silanes was prepared by reacting calculated quantities of methyltriacetoxysilane (18.40 g; 8.35 mM), methyltrimethoxysilane (14.30 g; 10.50 mM), tetramethoxysilane (3.60 g; 2.36 mM) and (3,3,3-trifluropropyl)methyl dimethoxysilane (0.37 g; 0.168 mM) to a reactor vessel, followed by sonication and an addition of isopropanol (50 ml; 65.31 mM). In a second reactor, a calculated quantity of sodium bicarbonate (1.0 g; 1.19 mM) was dissolved in 10 ml of water. The water was constantly stirred while sodium salt was added and then stirred every 2 h. The content of the second reactor was added to the content of the first and then sonicated for 30 min. In a third reactor, the calculated quantity of titanium isopropoxide (0.30 g; 0.105 mM) was sonicated in isopropanol (30 ml; 39.18 mM) for 30 min and added to the solution obtained in the above steps. A known quantity of isopropanol (50 ml; 65.31 mM) and dibutyltindilaurate (300 μg; 0.005 mM) was mixed separately in a reaction vessel and added to the solution obtained in the above steps. The entire solution was left for 30 min in ambient conditions before being used as a PSSQ coating precursor material.

2.2 Analysis of the PSSQ

The FTIR spectroscopy on solid PSSQ applied over aluminium metal was conducted using a Thermo Electron Nicolet Nexus 760 instrument attached to a Continuum microscope. The spectra were continuously recorded for at least 180 min in reflectance mode under the microscope to monitor the reaction species formed during various phases of the conversion/curing process. The spectra were analysed using Thermo Electron's Omnic and Series software. A minimum of 34 scans with a resolution of 4 cm^{-1} of the specimen were

employed for each spectrum. A blank background spectrum was collected prior to collecting a spectrum of the sample. Thermo SpectraCorr software was used to conduct 2D COS analysis.

The nanomechanical analysis was conducted on MTS Nanoindenter XP with a Berkovich diamond tip. The test samples were mounted with a thermoplastic polymer resin onto an aluminium stub. Fused silica was used as a standard calibration sample. The nanoindentation experiments were acquired with the help of TestWork 4 software from MTS instruments. The TestWork software exported the raw data files to the MS Excel software. The Excel data sheets were then imported on Analyst software from the MTS instrument for the data reduction. The Analyst-Excel files were finally used to plot the curves using Origin 7.5 software.

The PSSQ-coated aluminium specimens of 1x1 cm^2 were bonded to circular aluminium stubs using a thermoplastic resin. The aluminium specimens were cut from Al6061-T6 metal, which contained a native oxide layer. The specimens were polished to a mirror-like finish and stored in DryBox (with zero humidity) before the application of coating. The ultimate thickness of the hardened coating was approximately 1.5 μm (check the SEM image in supplement section). The stubs were then mounted on the Nanoindenter XP nano-positioning tray and tested. A Berkovich tip was used to perform three to six tests on each sample (identical one each for nanoindentation, nanoscratch and wear analysis) in different regions to achieve a reasonable representation of the nanomechanical properties of PSSQ. The three PSSQ-coated specimens were cured in identical ambient conditions and analysed every day until eight days of curing/hardening. For a separate test, a 10 ml glass vessel was filled with 5 ml liquid precursor to PSSQ and left to dry in ambient conditions for an extremely long period (approximately six months).

In a typical nanoscratch test, the indenter tip approaches the surface of the test sample at a rate of 30 nm/sec. Surface contact was set according to a pre-determined increase in measured stiffness,

S. The load applied to the indenter was then increased to a small profiling load of 20 μN and the original surface topography was scanned over the entire scratch path. When the indenter returned to the origin after the initial profiling scan, a pre-profile was performed up to the location of the desired scratch position. The indenter was then ramp-loaded while the translation stages moved the sample along the scratch path at a rate of 10 μm/sec. When the scratch length criteria were met, the indenter was unloaded to the profiling load and a post-profile scan was performed to the same length as the pre-profile scan. The pre- and post-profile segments were used to level the scratch cycle data. Once the post-profile was completed, the stages moved into position for the cross-profile segment and the cross-profile was initiated. The indenter was then withdrawn entirely and the sample was moved into position for the next experiment. In a typical wear test, the indenter tip approached the surface of the test sample at a rate of 10 nm/s. Surface contact was set according to a pre-determined increase in measured stiffness, S. The load applied to the indenter was then increased to a small profiling load of 50 μN and the original surface topography was scanned over the entire scratch path. When the indenter returned to the origin after the initial profiling scan, a pre-profile was performed up to the location of the desired scratch position. The indenter was then loaded to 8 mN. This load was held constant while the translation stages moved the sample along the scratch path at a rate of 50 μm/sec. When the scratch length criteria were met, the indenter was unloaded to the profiling load and a post-profile scan was performed to the same length as the pre-profile scan. The pre- and post-profile segments were used to level the scratch cycle data. Once the post-profile was completed, the stages moved the sample back to the origin (location of pre-profile). The indenter was loaded to the profiling load and the residual topography of the wear track was recorded. This combination of wear cycle and profiling was repeated for 10 cycles. After the completion of the wear cycles, a

cross-profile was performed. The indenter was then withdrawn entirely and the sample was moved into position for the next experiment.

The coated PSSQ morphology and scratched surface were analysed with a Hitachi S-4500, Scanning Electron Microscope (SEM). The atomic force microscopic (AFM) technique was used to study the surface morphology of the PSSQ hardened over a polished aluminium surface. The Bruker Multimode 8 operating in ScanAsyst™ mode was used to capture the surface topography. The 3D images were created using TrueMap™ software from TrueGage Surface Metrology.

3. RESULTS

The material displayed homogeneous spreading with near isotropic properties on curing. Hardness, modulus, nanoscratch and wear values were uniform with insignificant variation throughout the sample. The nanoscratch and wear properties presented here are not localized but a good representation of the entire surface.

3.1 Spectroscopic Analysis of the PSSQ

The curing/crosslinking reaction path in the material changes with the inclusion of foreign compounds. While the inclusion of a few participating chemical entities could accelerate the reaction, others could hinder the process. In an interesting study, Sheremetyeva et al. [45] introduced fluorine units into silane structures and noticed variation in the organizing ability of fluorine-containing fragments, leading to the formation of self-arranged hyperbranched dendrimers. The presence of fluorinated molecules in PSSQ, therefore, was deemed to trigger phase separation by forming isolated quasi-dendrimer sol particulates, as proposed in Schemes 1a, b. In our work we noticed that the addition of higher fluorine content in the backbone structure obstructed the curing in PSSQ. Steward et al. [46] did mention that the inductive effect

and molecular shielding arising from the trifluoromethyl group interferes with the hydrolysis and subsequent condensation reactions. Apparently, through iterative experiments, a smaller quantity of fluorinated moiety was identified to provide adequate surface characteristics to the PSSQ material. The FTIR spectral characteristics are significantly affected by the amount of fluorine in the material. Kim et al. [47] discovered that, on increasing the fluorine content in SiOF (υ_{Si-F}; 940 cm^{-1}) film, the SiOSi (υ_{Si-O}; 1,060 cm^{-1}) stretching vibration displayed blueshift, while increasing the carbon content in SiOC (υ_{Si-C}; 1,270 cm^{-1}) film showed redshift in the FTIR spectrum. The FTIR spectra shown in Figure 2a were continuously acquired for 60 min on PSSQ containing 10 wt. % fluorinated components in the precursor to observe the curing mechanism. The peak at 1,210 cm^{-1} representing $–CF_3$ was apparent in the spectra for this concentration. However, at lower fluorine concentration (1 wt. %), the 1,210 cm^{-1} peak was overlapped by other powerful broad peaks in the vicinity.

The group of spectral assignments shown in Figure 2b was acquired on PSSQ at regular intervals for eight days. Each day spectra were acquired on a fixed region for 60 minutes at the rate of one spectrum per minute. The spectra shown in Figure 2b for each day were selected from 0, 15, 30 and 45 minutes. During the initial curing period, a significant portion of hydrocarbon bands (including from the solvent) appeared predominantly and masked the other components. After day four, splitting of signals was recorded in the region between 1,100 and 800 cm^{-1}. The spectra assignments between 1,100 and 1,000 cm^{-1} displayed the construction of the coating's backbone. The –OH band between 3,400 and 3,100 cm^{-1} appeared even after prolonged curing time, suggesting that curing of silicones is a long-lasting process. The inset in Figure 2b shows the spectral assignments of major changes occurring in the bands between 900 and 1,200 cm^{-1} as a function of time. The increase in the peak intensity at 1,045 cm^{-1}, which is associated with the

formation of backbone structure, is accompanied by the reduction in broad peak centred at 1,125 cm^{-1}. Figure 3 shows an area of peaks centred at 915 cm^{-1}, 1,045 cm^{-1} and 1,090 cm^{-1}, corresponding to νSiOH, νSiOSi and $\nu SiOCH_3$ vibration modes respectively. The calculated area's curves were fitted with a linear equation where slopes indicate the amount of chemical species reacting as a function of time. It is apparent that the rate of formation of SiOSi is much higher compared with the consumption of methoxy and silanol groups. The 2D correlation spectroscopy (2D COS) postulated by Noda was adopted to study the time-sequence order of fundamental changes in the spectral assignments occurring during the chemical and physical processes. The 2D COS assists in analysing the complicated and overlapped bands by resolving the observed spectra. To achieve a correlation plot, the average spectrum was subtracted from the individual spectrum in the data set. The synchronous spectrum $\Phi(\nu_1, \nu_2)$ and asynchronous spectrum $\Psi(\nu_1, \nu_2)$ were calculated from equations as follows:

$$\Phi(\nu_1, \nu_2) = \frac{1}{n-1}\sum_{j=1}^{n} \widetilde{A}_j(\nu_1) \,.\, \widetilde{A}_j(\nu_2) \quad (1)$$

$$\Psi(\nu_1, \nu_2) = \frac{1}{n-1}\sum_{j=1}^{n} \widetilde{A}_j(\nu_1) \,.\, \sum_{k=1}^{n} N_{jk} \,.\widetilde{A}_j(\nu_2) \quad (2)$$

In equation (1) and (2), $\widetilde{A}_j(\nu)$ is the dynamic spectra, ν_1 and ν_2 are two independent frequencies, while *n* represents the number of spectra in calculation. The term N_{jk} in equation (2) is an element of the *j*-th row and *k*-th column in the Hilbert-Noda transformation matrix, defined as follows:

$$N_{jk} = \begin{cases} 0 & if\ j = k \\ \frac{1}{\pi(k-1)} & otherwise \end{cases} \quad (3)$$

The dynamic spectra $\widetilde{A}_j(\nu)$ is calculated as follows:

$$\widetilde{A_j}(\nu) = A_j(\nu) - \bar{A}(\nu) \quad (4)$$

where $\bar{A}(\nu)$ is the reference or averaged spectrum.

3.1.1 Analysis of hydrolysis and condensation region between 900 cm^{-1} and 1,045 cm^{-1}

Figure 4a shows a 3D synchronous fishnet plot; 2D synchronous plots of the coated PSSQ displayed as a contour map are shown in Figure 4b. The fishnet plot is useful in providing a better sense of the relative intensities between various correlation peaks, while the contour map could help in determining the maximum and minimum coordinates of the peak with greater accuracy. The time of curing was taken as external perturbation and 32 spectra were averaged for each spectrum. The spectra were collected continuously at a constant rate of 1 spectrum/min for 3 h. The reference spectrum was obtained by calculating the average of the entire spectral data set. The region with negative correlation intensity has been shaded in the 2D COS map. The three auto peaks were seen concentrated at (900, 900 cm^{-1}), (1,000, 1,000 cm^{-1}) and (1,100, 1,100 cm^{-1}), reflecting the intensity changes of bands as a function of time. These bands suggest that at least three chemical constituents have strong correlations. A positive cross peak was seen at (915, 1,090 cm^{-1}), while two negative cross peaks were seen at (915, 1,045 cm^{-1}) and (1,045, 1,090 cm^{-1}). The 3D asynchronous fishnet plot is shown in Figure 5a and 2D asynchronous plots of the coating displayed as a contour map are shown in Figure 5b. A strong positive cross peak was seen at spectral coordinate (915, 1,045 cm^{-1}), while a negative peak was located at (1,045, 1,090 cm^{-1}). Another relatively weaker positive cross peak was noticed at (1,090, 915 cm^{-1}).

On the synchronous map, the cross peak located at (915, 1,045 cm^{-1}) is negative. This means that the intensities of the two peaks are changing in opposite directions. In addition, on the asynchronous map, the cross peak located at (915, 1,045 cm^{-1}) is positive, which means that the

peak 915 cm^{-1} precedes the peak at 1,045 cm^{-1}, i.e., SiOSi (1,045 cm^{-1}) is formed at the consumption of SiOH (915 cm^{-1}). The synchronous cross peak at (1,045, 1,090 cm^{-1}) is negative, suggesting that the intensities of these two peaks change in opposite directions. However, the asynchronous cross peak at (1,045, 1,090 cm^{-1}) is also negative, suggesting that the intensities of 1,045 cm^{-1} and 1,090 cm^{-1} change in the same direction. In addition, the peak at 1,045 cm^{-1} (SiOSi) follows the peak at 1,090 cm^{-1} ($SiOCH_3$). The synchronous cross peak at (915, 1,090 cm^{-1}) is positive, suggesting that the intensities of these bands in the data set change in the same direction. However, the asynchronous cross peak at (915, 1,090 cm^{-1}) is negative, suggesting that 915 cm^{-1} (SiOH) follows the peak 1,090 cm^{-1} ($SiOCH_3$). This is true, as Si (-OH) is formed at the consumption of Si (-OCH_3). The changes in intensity patterns observed here are similar to those observed in Figure 3.

3.1.2 Analysis of hydrogen bonding region between 3,600 cm^{-1} and 3,800 cm^{-1}

The 3D fishnet plot and 2D map of synchronous correlation are displayed in Figure 6a and 6b, while those of asynchronous correlation are displayed in Figure 7a and 7b. The synchronous 2D COS map for the region between 3,600 and 3,800 cm^{-1} shown in Figure 6b displays two strong auto peaks and one moderate (3,648, 3,648 cm^{-1}), (3,674, 3,674 cm^{-1}) and (3,785, 3,785 cm^{-1}). On the synchronous map (Figure 6b), the strong cross peak (3,648, 3,674 cm^{-1}) is positive, while the asynchronous (Figure 7b) cross peak (3,648, 3,674 cm^{-1}) is negative. This suggests that peak intensities at 3,648 cm^{-1} and 3,674 cm^{-1} are changing in opposite directions and that 3,648 cm^{-1} follows the peak at 3,674 cm^{-1}. Similarly, the weak cross peak (3,648, 3,785 cm^{-1}) is positive, while the asynchronous cross peak is negative. On reversing our assumption for the synchronous cross peak, it appears that the band at 3,648 cm^{-1} and 3,785 cm^{-1} changes in the opposite direction. In addition, the band at 3,648 cm^{-1} follows that at 3,785 cm^{-1}. The moderate

synchronous cross peak (3,674, 378 cm^{-1}) is positive, while the asynchronous cross peak (3,674, 3,785 cm^{-1}) is negative. On reversing our assumption for the synchronous cross peak, it is clear that bond 3,674 cm^{-1} and 3,785 cm^{-1} change in opposite directions. Moreover, the bond intensity at 6,374 cm^{-1} follows that at 3,785 cm^{-1}. The band intensity at 3,648 cm^{-1} is assigned to the free clustered water (molecular water), while 3,674 cm^{-1} is designated to weakly bound water (adsorbed water) [48]. The strong hydrogen bonded water (SiO••••H••••OH_2) is seen at 3,785 cm^{-1}.

3.2 Condensation and volume collapse in the PSSQ

As mentioned above, the aluminum surfaces were polished to remove the inert oxide surface. The polished coupons containing freshly exposed aluminum hydroxide groups were kept in drybox (in absence of humidity) until coated. Such aluminum coupons containing active hydroxyl groups tend to react with the hydroxyl groups from the coating to perform permanent covalent linkages. After overnight (24 h) hardening of coating ($PSSQ_1$) in ambient conditions, the surface roughness was significantly high and could not be captured with AFM. The average original surface roughness was in the order of 65 nm. Figure 8 shows the displacement of the Berkovich head into the coating surface plotted as a function of scratch distance. The original surface morphology and the final surface morphology obtained after the completion of the nanoscratch test is shown, along with the penetration curve. Critical load (CL) needed for the fracture can be defined as the point on the penetration curve that matches the point of deflection in final surface morphology from the original surface morphology. A wave pattern was observed in the scratched surface morphology after nanoindenter head slides for 190 μm; however, the first sign of crack was observed after 255 μm scratched distance. Surface damage occurred after critical load of 6.30 mN after 673 nm penetration depth and significant surface roughness was observed thereafter. The Coefficient of Friction (COF) was also recorded as a function of scratch

distance and displayed in Figure 9. It is worth mentioning that COF is a dynamical value subject to the influence of asperities on the surface, which after extended running-in stabilizes with the loss of asperities. After 24 h of hardening, the COF value was exceptionally high and inconsistent, therefore was not displayed in this curve.

Sakai [49] mentioned that the energy required for elastic and plastic deformation in an engineering material can be calculated from the load vs displacement (LD) curve in a nanoindentation experiment. A typical LD hysteresis cycle can be divided into three energy planes: elastic energy (U_{EE}), plastic energy (U_{PE}) and total energy (U_{TE}). The area under the loading curve demonstrates the U_{TE} value and the area under the unloading curve gives the U_{EE} value. The difference of $U_{TE} - U_{EE}$ represents the permanent plastic deformation energy (U_{PE}) and is the region confined between the loading and unloading curves. The three energies calculated from the LD curves obtained as a function of curing time are shown in Figure 10. The U_{EE} attains plateau with time before becoming stagnant. Interestingly, PSSQ hardened for 192 h displayed high U_{PE}, while this value was significantly low after extended curing time. An interesting periodic energy fluctuation was observed in the U_{TE} and U_{PE} as a function of curing time. The U_{PE} values were relatively low after 48 h, 144 h and inf (infinite) time curing, which may be related to the progressive hydrolysis and subsequent (poly)condensation or crosslinking reactions in succeeding layers of PSSQ.

The surface topography after 48 h ($PSSQ_2$) of ambient condition hardening is shown in Figure 11. The distribution of hills and valleys can be seen in the 500 nm scanned area. The average surface roughness (S_a) determined by AFM was 1.7 nm, while the root mean square roughness (S_q) was 2.1 nm. The maximum depth of the valley (S_v) was 7.0 nm, while the maximum peak height (S_p) was 7.1 nm. The average surface roughness as calculated with the nanoindenter tip

decreased significantly to 35 nm. Figure 12a shows the nanoscratch profile. The indenter slid until 371 μm, penetrated to approximately 1,267 nm and fractured the coated surface at 10.9 mN CL. In the wear cycle shown in Figure 12b, significant enhancement in surface roughness appeared after the first wear cycle. On comparison with the top layer, larger surface deformation was seen in the second layer, while much less deformation occurred within succeeding layers of the coated surface, probably due to the surface-dominated confined orientation and curing of the material. It appeared that a few layers beneath the top surface were not fully cured, probably due to clustering of water molecules. The wear test was repeated to confirm the finding and similar results were obtained in both the tests. The maximum wear track deformation was approximately 850 μ^2, which occurred in the final wear cycle, while the average displacement into the surface was 2,000 nm. The fluctuation in COF during the nanoscratch stipulates the inherent roughness on the surface. The COF value was 0.47 at CL, which showed a tendency to decrease with the curing of the film (Figure 9).

The surface topographical image of PSSQ coating hardened for 96 h ($PSSQ_4$) is shown in Figure 13a. A significant reduction in hills and valleys was recorded in the area of scan. The hills converted to sharp peaks originating due to the in-situ generation of nanoparticles. The S_a decreased to 0.35 nm and S_q to 0.76 nm. Similar reduction was observed for S_v = 2.5 nm and S_q = 6.9 nm. The average surface roughness as calculated through nanoindenter tip was approximately 31 nm, a value similar to that obtained after 48 h of curing. In this test (Figure 13a), the indenter slid until 320 μm, penetrated to approximately 1,279 nm and fractured the coated surface at 13 mN CL. Although the CL was higher after 48 h curing, the slide distance and depth of penetration at CL was lower. This indicates that the coating was not uniformly hardened in all the regions. In the wear test shown in Figure 13b, the first sign of surface damage

appeared after completion of the fifth cycle. On observing the wear track deformation, the highest deformation was recorded between the first and second layer. The deformation was uniform in the other remaining layers and the maximum wear track deformation was 563 μ^2, which occurred in the final cycle. The first sign of coating failure was recorded in the sixth wear cycle and the average displacement into the surface was 870 nm, indicating enhanced crosslinking density between the coating layers. At this stage, the COF curve gained uniformity over the scratched distance. The continuous incensement in COF value with scratch distance revealed the higher cohesive strength within coating layers. The COF was 0.34 at CL, a value that was 13 % less than 48 h hardening of PSSQ.

As described earlier, the macromolecular segments gradually condensed over time and the nanoparticles appeared distinctly isolated after 144 h of hardening. The surface morphology after 144 h ($PSSQ_6$) of hardening showed that roughness decreased to a noticeable value. The recorded reduction was S_a = 0.24 nm and S_q = 0.31 nm, while S_v = 1.63 and S_p = 2.94 nm. The average surface roughness after 144 h of curing was approximately 38 nm. The nanoscratch test shown in Figure 14a displayed the fracture that occurred at 17 mN CL, a value higher than that obtained after 96 h of crosslinking. The indenter head travelled until 385 μm and penetrated to 1,449 nm when fracture occurred. In the wear test shown in Figure 14b, the wear track deformation was uniform until six wear cycles and fracture appeared at the beginning of the seventh cycle. The maximum wear track deformation was 531 μ^2, which occurred in the eighth cycle. The displacement into the surface in each cycle was approximately 900 nm and the maximum displacement into the surface (950 nm) was observed in the eighth wear cycle. Significant damage to the surface was recorded in the 10th wear cycle. Surprisingly, here, the COF value at CL remained similar to that observed after 144 h hardening of coating.

Enhanced condensation of sol particulates led to volume collapse in the 3D network. The pronounced appearance of nanoparticles could be visualized as the surface roughness decreased (Figure 15). After 192 h ($PSSQ_8$), the recorded reduction in roughness parameters was S_a = 0.26 nm and S_q = 0.40 nm, while S_v = 1.1 nm and S_p = 3.2 nm. When determined from the nanoindenter, the average surface roughness after 192 h of curing was approximately 30 nm. The nanoscratch test shown in Figure 16a displayed the fracture that occurred at 17 mN CL, a value similar to that obtained after six days of crosslinking. In this case, the indenter head travelled until 525 μm and penetrated to 1,425 nm when fracture occurred. Although the indenter head travelled for a longer distance than the previous case, the depth of penetration was approximately similar, suggesting that the coating reached its optimum hardness that could be achieved in ambient curing conditions. The coating, however, continues to harden throughout the life of the material. In the wear test shown in Figure 16b, the wear track deformation was uniform until eight wear cycles and cracking was prominent at the beginning of the ninth cycle. The maximum wear track deformation was 552 μ^2 observed in the last (i.e., 10th) wear cycle. The average displacement into the surface gradually increased with each wear cycle and the maximum value (i.e., 935 nm) was observed in the final wear cycle. The nanoindentation hardness value did not show noticeable change on extended hardening; therefore, periodic nanoscratch tests were not performed on the PSSQ coating material cured beyond 192 h. It was, however, enthralling to note that the COF value at CL decreased to 0.23, a more than 60 % drop from the 48 h curing time.

The surface topography of significantly long hardened $PSSQ_{in}$ (described in detail in the following section) was different from those that were cured over metal substrate (Figure 17). The Sa (0.56 nm) and Sq (0.71 nm) values were remarkably higher than previous cases. Similarly, Sv

(3.8 nm) and Sp (4.4 nm) values were higher in this case. Originally, the average surface roughness of the fully hardened material was approximately 75 nm. However, after polishing with nanodiamond solution, the average surface roughness was approximately 10 nm. The nanoscratch test shown in Figure 18a displayed a tiny fracture that occurred at 30 mN CL. In this case, the indenter head travelled until 510 μm and penetrated to 1,937 nm when fracture occurred. Although the sample appeared dense, the indenter tip penetrated to a much lower depth at the point of fracture. In the wear test shown in Figure 18b, the wear track deformation was uniform until six wear cycles. The sample surface was not flat; hence, prediction of surface roughness was difficult. The first sign of failure appeared in the seventh wear cycle with maximum wear track deformation of 707 μ^2 in the third wear cycle. The average displacement into the surface was mostly uniform in each wear cycle with marginal reduction in each progressive wear cycle. A relatively higher friction (Figure 9) was noticed in the initial stages of the scratch, which levelled down to a uniform value. The COF value at CL was 0.34, similar to that obtained for curing until 144 h.

4. THE CORRELATION

Solvent used here inadvertently contained traces of bound water and also that added in the reaction vessel to induce hydrolysis and generate an activated sol may not be sufficient to hydrolyse the entire alkoxy (-OCH_3 or OMe) and acetoxy (-$OOCCH_3$ or OAc) groups in silanes. As shown in Figure 18a, approximately 32 % of labile groups remained unhydrolysed from the amount of water added in the initial stages of the reaction. On addition of water in the reaction mixture, an activated sol is produced, having equilibrium between hydrolysed and unhydrolysed silanes, along with the generated methanol and acetic acid. The FTIR spectrum recorded on elute during the early stages of reaction displayed sharp bending bands in the region between 1,260

and 1,195 cm^{-1} and 1,770 and 1,725 cm^{-1}, representing the SiOAc linkages. These two bands are reported sensitive to the number of connected –OAc groups. It was determined that the bending vibration band between 1,260 and 1,195 cm^{-1} shows blueshift, while the stretching vibration band between 1,770 and 1,725 cm^{-1} showed redshift with each leaving OAc group. The formation of corresponding free acetic acid appears at δ_s 1,412 cm^{-1} (COO^-), δ_{as} 1,550 cm^{-1} (COO^-) and ν1,710 cm^{-1} (COOH). The conversion of the OMe group to methanol is difficult to observe as bending vibration bands in the region between 1,100 and 1,000 cm^{-1} are often masked, due to the presence of stronger bands from silanes (-OSi). However, the cross peaks on the 2DCorr map provided deconvolution to draw insight into the competing reaction processes. On investigating the regime between 1,200 and 800 cm^{-1}, it is apparent that the easy formation of silanol is the driving force behind the conversion of the OMe group into methanol. Stronger bending vibration from primary alcohol appears mostly around 1,050 cm^{-1}; therefore a contour (1,010, 1,100 cm^{-1}) could be ascribed to the probable free methanol. The probability of the existence of free methanol and acetic acid is considerably higher during the initial phases of reaction. The possibility of such an existence decreases with time due to the incoming water molecules forming hydrogen bonding with these free moieties. The slope of the area curve representing SiOSi peak at 1,035 cm^{-1} in Figure 3 is much larger than 915 cm^{-1}, suggesting a rapid conversion of silanol (-SiOH) to -SiOSi backbone. Conversely, the backbone formation is the driving force for the rapid condensation of silanol and the release of water molecules. The remnant methanol and acetic acid (RMA) molecules have a natural tendency to perform hydrogen bonding (HOB) with the Released Water Molecules (RWM). This means that the RWM may no longer be available for the hydrolysis of remnant SiOAc and SiOMe. On considering the mole stoichiometric ratio in the reaction shown in Figure 18a, it

appears that, for each macromolecule formation, 12 molecules of RMA will be released along with six RWM. As each water molecule could form up to four HBs, both inter- as well as intramolecular HOBs will hence dominate the reaction process.

Vernon et al. [50] demonstrated the formation of several three-dimensional cyclic water clusters between 3,715 and 3,545 cm^{-1}. The free and bound water molecules in their work displayed significantly different spectral assignments. The analysis of synchronous and asynchronous 2DCorr maps of the regime between 3,800 cm^{-1} and 3,600 cm^{-1} suggested that water inside the PSSQ macromolecular segments existed in three different states. As mentioned earlier, the appearance of contour at 3,648 cm^{-1} represents clustered water molecules with intramolecular HOBs. The clustering of water arises as a result of water generated during the condensation of silanol, which is absorbed during the moisture curing of the material. Another contour appearing at 3,674 cm^{-1} is due to the weakly bound water as a result of London Dispersion Forces (LDF), while the contour of the third form of water visible at 3,785 cm^{-1} is mostly due to intermolecular HB hydroxyl moieties in silanes or silanols. On observing the cross peaks during the moisture curing of PSSQ, it is apparent that the incoming water molecule is initially dissolved inside the interstitial sites of the material.

Assender et al. [51] identified that self-assembly of reactive particulates is deemed responsible for the physicomechanical properties of the coated surface. While adequate roughness on the surface may enhance the wear resistance in some instances, no direct correlation exists between the surface roughness and wear in material. In case of PSSQ, the surface roughness after overnight hardening was significantly high and, on conducting nanoscratch, the material failed abruptly at extremely low load value and lateral force. Moreover, high plastic deformation incurred with significantly high pileup (632 nm) of material. This suggests that hydrolysis and the subsequent

condensation reaction was underway at this stage and an attempt to determine the wear resistance of material would not return any meaningful result. Surface roughness measured with the nanoindenter suggested that, after prolonged hardening for two days (i.e., 48 h), surface roughness drastically reduced. However, on observing the surface under AFM, phase-separated domains were distinctly apparent. At this stage, the sol particulates coalesced due to the hydrolysis reaction but did not reach the stage of adequate condensation. The energy analysis also suggested that U_{PE} (~28,000 μJ) was significantly high compared with U_{EE} (~12,000 μJ) as a result of ongoing hydrolysis and formation of amorphous domains. On subsequent condensation, these domains align to form a more elastic network.

The nanoscratch profile appeared relatively smooth compared with the former case, with approximately 45 % increase in fracture strength. A significant increment in lateral force and a noticeable drop in plastic deformation was recorded at this stage. In the wear test, the initial wear cycles were rough, suggesting that the layers below the surface did not freeze due to inefficient condensation and hardening. The formation of discrete nanoparticles out of phase-separated islands were observed on extended hardening. These nanoparticles were homogeneously distributed over the surface and bulk of the film. A broad size distribution was recorded for these nanoparticles which is apparent in Figure 9 and surface morphology in the nanoscratch curve. After 96 h, the surface roughness declined by 86 % compared with that after 48 h of hardening, along with a similar drop in average depth and height of valley. It appeared that a significant amount of volume collapsed while drying, which could be attributed to the overall changes in the surface morphology. The nanoscratch test reflected similar results, with 20 % increment in critical load to fracture and approximately 12 % increment in lateral force at critical load, with more than 40 % reduction in plastic deformation. It is, however, interesting to note that depth at

critical load remained practically the same between 48 h and 96 h hardening, indicating that the crosslinking reaction was stronger in X and Y directions of surface, yet relatively weaker in Z direction. This is probably due to the hindered in-diffusion of water molecules needed for the hydrolysis and subsequent condensation of silanes [17]. The premise is prominent in the energy analysis, where U_{PE} was almost identical after 48 h and 96 h hardening. The U_{EE}, however, increased, as some of the domains aligned to enhance the work needed for elastic deformation. Studies conducted by Bunker et al. [52] have demonstrated the thermodynamic preference of formation of a top dense layer, which creates a tough barrier for the incoming water molecules. The wear analysis on PSSQ revealed features that were significantly different from 48 hours of hardening. On observing the track deformations, it appears that the wear pattern was uniform between different layers of the coating. Intriguingly, the average displacement into the surface dropped by 56 % during this time, while cycles to fracture increased three times.

No significant difference was observed in PSSQ from a morphological perspective after 144 h of hardening. Although the average surface roughness was similar to that after 96 h, the critical load to fracture during the nanoscratch test increased by 31 %, while lateral force at critical load was 26 % higher. Moreover, the friction coefficient decreased by 21 %, along with a similar reduction in plastic deformation. The first wear cycle profile at this stage was similar to the original surface morphology, suggesting that coating was sufficiently hard at this point and no significant surface deformation was recorded. It is interesting to note that repeated wear cycles (shown in inset) at this stage did not result in substantial surface damages. The first sign of severe surface fracture appeared in the seventh wear cycle.

Any noticeable difference in average surface roughness was not observed after 192 h compared with 144 h. The nanoscopic observations displayed connected phase-separated islands with

scattered nanoparticles. It appears that the values of maximum depth of valley and root mean square roughness remained unaffected by curing time beyond 144 h. The critical load at fracture did not change after 144 h, but the amount of plastic deformation decreased by 11 %. It is interesting to note that the friction coefficient at critical load decreased by 32 % during this time. The energy analysis suggested that U_{EE} decreased slightly from 144 h with a significant increment in U_{PE}. The work done for plastic deformation at this stage was approximately two times more ($U_{PE} = 2U_{EE}$) than for elastic deformation. On observing the nanoscratch under SEM, it appeared that the first instance of coating crack observed after the indenter head moved to 150 μm, while the second crack was seen after 325 μm displacement. In comparison with the original surface morphology in the nanoscratch curve, it is clear that the coating chipped off the surface during these events, probably due to coating defects or residual stress accumulation in those regimes. The actual fracture accrued after 525 μm displacement. Further, comparing the scratch under the SEM, it appears that the coating chipped off twice before the actual fracture occurred. The coating's inherent defects due to residual stresses and conglomeration of nanoparticles could be held responsible for such an effect. A constitutive molecular model in Figure 19 demonstrates the adhesion of PSSQ coating to the metal surface via covalent bonding. The coating lift-off (or chipping) occurs as a result of internal residual stresses in extensively crosslinked structures. On subjection to wear test at this stage, uniform track deformation was recorded in each wear cycle, with the first sign of wear-induced cracking appearing in the eighth cycle.

Wallace and Hench [53] demonstrated various process parameters that affect the final characteristics of sol-gel routed material. Such a premise motivated us to cure the precursor to PSSQ in a glass container so that alignments of macromolecular chains remain immune to the metallic surface orientation. After extended hardening of the monolithic sample, the surface

morphology was slightly different from the samples cured on the metal surfaces. The polymeric chains in coating cured in a confined glass vessel pass through a series of surface-mediated constraints acting in X, Y and Z directions, which forces macromolecules to align in pre-oriented patterns biased to the boundary conditions. The confined boundary conditions result in curved surface morphology, in contrast to flat surface morphology in cases of curing over an open 2D surface. Moreover, rigid boundary conditions push polymer chains to confine in relatively smaller volume, leading to the super-dense structure appearing in Figure 17. The effect of the condensed surface was prominent in the nanoscratch analysis conducted on the polished sample. An increment of approximately 13 % in CL to fracture was recorded, along with twice the enhancement in lateral force at CL. The COF, however, remained similar to that after 144 h of curing. Surprisingly, the original surface roughness as proved using nanoindenter head and AFM was found to be higher than after 192 h of hardening. It is possible that the polymeric chain tends to perturb in the Z axis due to the confined volume and restriction of motion in X and Y directions. There was negligible plastic deformation during this test.

The polished sample used in the nanoscratch test loses the natural surface texture that may be critical in wear analysis studies. Original, cured monolithic PSSQ coating that displayed curved surface morphology was utilized for the wear test. A vast difference was observed in initial and final surface topography, which represented the loss of material during wear cycles. Initially, signs of cracking were observed from the first wear cycle. The material, however, deformed uniformly in the following cycles. Moderate to severe damage was observed from the seventh cycle onwards, which is similar to that observed after 144 h of hardening. This established that optimum and adequate curing of PSSQ can be achieved after seven days in ambient conditions. The energy analysis displayed distinctly different behaviour compared with other curing times.

The U_{EE} was close to that observed after 192 h, but the U_{PE} decreased to a significantly lower value. This endorses our argument that material attains an elastic nature after an extended period of curing/hardening. The periodic fluctuation in U_{PE} values in Figure 10 strengthens our hypothesis on absorption, clustering, percolation and consumption of water molecules in the matrix. The plasticity increases after 96 h with the absorption of water molecules in succeeding layers and the subsequent hydrolysis of alkoxysilanes to silanols. The elasticity increases at the consumption of some of these plasticized domains, which align through condensation to impart rigidity in backbone structure. Eventually, after extended time hardening, the plastic domains are drastically reduced and the material attains relatively high elasticity.

5. SUMMARY AND CONCLUSIONS

The hydrolysis and subsequent condensation reaction in multilayer PSSQ coating material largely depends on the number of water molecules present around each hydrolysing entity. It was discovered that, while surplus amount of water could contribute to the retarding condensation reaction, the adequate water would impede other competing reactions along with the main reaction. The 2D correlation spectroscopy assisted in devising the premise that inter- and intramolecular hydrogen bonding dominated reaction conditions and also conflicted with the condensation and silanol addition reaction. It was reaffirmed that the spontaneous formation of siloxane backbone was the driving force behind condensing silanols. Progressively changing surface morphology as a result of curing affected the COF and, consequently, wear resistance in the material. In case of PSSQ hardened over aluminium surface, COF decreased up to 50% while CL increased up to 35%. Similarly, a significant improvement (up to 100%) was observed in wear resistant with the passage of time. Work done on the deformation of plasticized domains oscillated as a function of time and the material consumed the amorphous domains to attain high

elastic characteristics. The elastic energy of the material increased to approximately 35% while the plastic energy increased to 29%. Concisely, it was apparent from the study that an appropriate number of water molecules in a reaction give rise to adequate surface roughness, leading to a desired wear resistance in the PSSQ coating material.

ASSOCIATED CONTENT

Supporting Information :

Figure S1: Load Vs displacement curve displaying loading and unloading cycle after 48 h of hardening. No inconsistency was observed in the loading cycle. **Figure S2**: Load Vs displacement curve displaying loading and unloading cycle after 96 h of hardening. No inconsistency was observed in the loading cycle. **Figure S3**: Load Vs displacement curve displaying loading and unloading cycle after 144 h of hardening. No inconsistency was observed in the loading cycle. **Figure S4**: Load Vs displacement curve displaying loading and unloading cycle after 192 h of hardening. There was slight deflection in the loading cycle suggesting that coating cracked or surface chipped off on application of high load. Such a data can be utilized for the calculation of fracture energy in coatings. **Figure S5**: Load Vs displacement curve displaying loading and unloading cycle after inf h of hardening. No inconsistency was observed in the loading cycle. The loading and unloading curves were close to each other suggesting negligible plastic deformation and high elasticity in the material. **Figure S6:** The SEM image of the impression after nanoindentation test. A crack developed on the coating after indenter head was withdrawn off the surface. **Figure S7:** The SEM image of the scratch showing the cracking and delamintation in the coating over metal surface. The estimated thickness of the coating was 1.52 μm. **Figure S8:** The SEM image of wear analysis on PSSQ. The removal of different layers in coating can be seen along with the cracks on the surface. **Table S1:** Various parameters derived from the analysis on PSSQ as a function of time. This material is available free of charge via the Internet at http://pubs.acs.org

AUTHOR INFORMATION

Corresponding Author

*Email: tiwari@hawaii.edu

Present Address

Pantheon Chemical Inc., Phoenix, 85027, AZ, USA

Notes

The authors declare no competing financial interest.

ACKNOWLEDGEMENTS

The authors (AT and LHH) are grateful for support from the US Marine Corps (USMC) Corrosion Prevention and Control Program and the Department of Energy, Oak Ridge National Laboratory (Contract #4000106469), for the project entitled "Pacific Rim Corrosion Assessment and Mitigation Program (PacRimCAMP)".

REFERENCES

1. Schwarz, U. D., Tracking antiwear film formation. *Science* **2015,** 348, 40-41.
2. Koren, E.; Lörtscher, E.; Rawlings, C.; Knoll, A. W.; Duerig, U., Adhesion and friction in mesoscopic graphite contacts. *Science* **2015,** 348 , 679-683.
3. Liao, Y.; Pourzal, R.; Wimmer, M. A.; Jacobs, J. J.; Fischer, A.; Marks, L. D., Graphitic Tribological Layers in Metal-on-Metal Hip Replacements. *Science* **2011,** 334, 1687-1690.
4. Maeda, N.; Chen, N.; Tirrell, M.; Israelachvili, J. N., Adhesion and Friction Mechanisms of Polymer-on-Polymer Surfaces. *Science* **2002,** 297, 379-382.
5. Liley, M.; Gourdon, D. F.-S.; Stamou, D. F.-M.; Meseth, U. F.-F.; Fischer, T. F.-L.; Lautz, C. F.-S.; Stahlberg, H. F.-V.; Vogel, H. F.-B.; Burnham, N. F.-D.; Duschl, C., - Friction anisotropy and asymmetry of a compliant monolayer induced by a small molecular tilt. *Science* **1998,** 280, 273-5.
6. Hone, J.; Carpick, R. W., Slippery when dry. *Science* **2015,** 348, 1087-1088.
7. Sheehan, P. E.; Lieber, C. M., Nanotribology and Nanofabrication of MoO3 Structures by Atomic Force Microscopy. *Science* **1996,** 272, 1158-1161.

8. Gosvami, N. N.; Bares, J. A.; Mangolini, F.; Konicek, A. R.; Yablon, D. G.; Carpick, R. W., Mechanisms of antiwear tribofilm growth revealed in situ by single-asperity sliding contacts. *Science* **2015,** 348, 102-106.

9. Tiwari, A., *Nanomechanical Analysis of High Performance Materials*. 1 ed.; Springer: Netherlands, 2014; p 345.

10. Tuteja, A.; Choi, W.; Ma, M.; Mabry, J. M.; Mazzella, S. A.; Rutledge, G. C.; McKinley, G. H.; Cohen, R. E., Designing Superoleophobic Surfaces. *Science* **2007,** 318, 1618-1622.

11. Landskron, K.; Hatton, B. D.; Perovic, D. D.; Ozin, G. A., Periodic Mesoporous Organosilicas Containing Interconnected [Si(CH2)]3 Rings. *Science* **2003,** 302, 266-269.

12. Shea, K. J.; Loy, D. A., Bridged Polysilsesquioxanes. Molecular-Engineered Hybrid Organic−Inorganic Materials. *Chem. Mater.* **2001,** 13, 3306-3319.

13. Loy, D. A.; Shea, K. J., Bridged Polysilsesquioxanes. Highly Porous Hybrid Organic-Inorganic Materials. *Chem. Rev.* **1995,** 95, 1431-1442.

14. Barton, T. J.; Bull, L. M.; Klemperer, W. G.; Loy, D. A.; McEnaney, B.; Misono, M.; Monson, P. A.; Pez, G.; Scherer, G. W.; Vartuli, J. C.; Yaghi, O. M., Tailored Porous Materials. *Chem. Mater.* **1999,** 11, 2633-2656.

15. Loy, D. A.; Mather, B.; Straumanis, A. R.; Baugher, C.; Schneider, D. A.; Sanchez, A.; Shea, K. J., Effect of pH on the Gelation Time of Hexylene-Bridged Polysilsesquioxanes. *Chem.Mater.* **2004,** 16, 2041-2043.

16. Aoki, Y.; Norisuye, T.; Tran-Cong-Miyata, Q.; Nomura, S.; Sugimoto, T., Dynamic Light Scattering Studies on Network Formation of Bridged Polysilsesquioxanes Catalyzed by Polyoxometalates. *Macromolecules* **2003,** 36, 9935-9942.

17. Brinker, C. J.; Scherer, G. W., *Sol–gel science, the physics and chemistry of sol–gel processing*. Academic Press: Boston, 1990.

18. Mammeri, F.; Bourhis, E. L.; Rozes, L.; Sanchez, C., Mechanical properties of hybrid organic-inorganic materials. *J. Mater. Chem.* **2005,** 15, 3787-3811.

19. Cordes, D. B.; Lickiss, P. D.; Rataboul, F., Recent Developments in the Chemistry of Cubic Polyhedral Oligosilsesquioxanes. *Chem. Rev.* **2010,** 110, 2081-2173.

20. Baney, R. H.; Itoh, M.; Sakakibara, A.; Suzuki, T., Silsesquioxanes. *Chem. Rev.* **1995,** 95, 1409-1430.

21. Li, G.; Wang, L.; Ni, H.; Pittman, C., Jr., Polyhedral Oligomeric Silsesquioxane (POSS) Polymers and Copolymers: A Review. *J. Inorg. Organomet. Polym.* **2001,** 11, 123-154.

22. Wang, F.; Lu, X.; He, C., Some recent developments of polyhedral oligomeric silsesquioxane (POSS)-based polymeric materials. *J. Mater. Chem.* **2011,** 21, 2775-2782.

23. Liu, C.; Lambert, J. B.; Fu, L., A Novel Family of Ordered, Mesoporous Inorganic/Organic Hybrid Polymers Containing Covalently and Multiply Bound Microporous Organic Hosts. *J. Am. Chem. Soc.* **2003,** 125, 6452-6461.

24. Brinker, C. J., Hydrolysis and condensation of silicates: Effects on structure. *J. Non-Cryst. Solids* **1988,** 100, 31-50.

25. Schmidt, H.; Scholze, H.; Kaiser, A., Principles of hydrolysis and condensation reaction of alkoxysilanes. *J. Non-Cryst. Solids* **1984,** 63, 1-11.

26. Assink, R. A.; Kay, B. D., Sol-gel kinetics I. Functional group kinetics. *J. Non-Cryst. Solids* **1988,** 99, 359-370.

27. Kobayashi, T.; Shishido, R.; Mizuse, K.; Fujii, A.; Kuo, J.-L., Structures of hydrogen bond networks formed by a few tens of methanol molecules in the gas phase: size-

selective infrared spectroscopy of neutral and protonated methanol clusters. *Phys. Chem. Chem. Phys.* **2013,** 15, 9523-9530.

28. Mizuse, K.; Mikami, N.; Fujii, A., Infrared Spectra and Hydrogen-Bonded Network Structures of Large Protonated Water Clusters H+(H2O)n (n=20–200). *Angew. Chem., Int. Ed.* **2010,** 49, 10119-10122.

29. Miyazaki, M.; Fujii, A.; Ebata, T.; Mikami, N., Infrared Spectroscopic Evidence for Protonated Water Clusters Forming Nanoscale Cages. *Science* **2004,** 304, 1134-1137.

30. Depla, A.; Verheyen, E.; Veyfeyken, A.; Van Houteghem, M.; Houthoofd, K.; Van Speybroeck, V.; Waroquier, M.; Kirschhock, C. E. A.; Martens, J. A., UV-Raman and 29Si NMR Spectroscopy Investigation of the Nature of Silicate Oligomers Formed by Acid Catalyzed Hydrolysis and Polycondensation of Tetramethylorthosilicate. *J. Phys. Chem. C* **2011,** 115, 11077-11088.

31. Schottner, G., Hybrid Sol−Gel-Derived Polymers: Applications of Multifunctional Materials. *Chem. Mater.* **2001,** 13, 3422-3435.

32. Pouxviel, J. C.; Boilot, J. P.; Beloeil, J. C.; Lallemand, J. Y., NMR study of the sol/gel polymerization. *J. Non-Cryst. Solids* **1987,** 89, 345-360.

33. Khamova, T. V.; Shilova, O. A.; Kopitsa, G. P.; Almásy, L.; Rosta, L., Small-angle neutron scattering study of the mesostructure of bioactive coatings for stone materials based on nanodiamond-modified epoxy siloxane sols. *Phys. Solid State* **2014,** 56, 105-113.

34. Black, E. P.; Ulibarri, T. A.; Beaucage, G.; Schaefer, D. W.; Roger, A. A.; Bergstrom, D. F.; Giwa-Agbomeirele, P. A.; Burns, G. T., Sol-Gel-Derived Silica-Siloxane Composite

Materials. In *Hybrid Organic-Inorganic Composites*, American Chemical Society: 1995; Vol. 585, pp 237-246.

35. Cheng, Y.-H.; Chen, W.-P.; Shen, Z.; Fan, X.-H.; Zhu, M.-F.; Zhou, Q.-F., Influences of Hydrogen Bonding and Peripheral Chain Length on Mesophase Structures of Mesogen-Jacketed Liquid Crystalline Polymers with Amide Side-Chain Linkages. *Macromolecules* **2011,** 44, 1429-1437.

36. Noda, I., Generalized Two-Dimensional Correlation Method Applicable to Infrared, Raman, and Other Types of Spectroscopy. *Appl. Spectrosc.* **1993,** 47, 1329-1336.

37. Noda, I.; Ozaki, Y., *Two-Dimensional Correlation Spectroscopy: Applications in Vibrational and Optical Spectroscopy*. Wiley: New York, 2004; p 310.

38. Koeppe, B.; Tolstoy, P. M.; Guo, J.; Nibbering, E. T. J.; Elsaesser, T., Two-Dimensional UV–vis/NMR Correlation Spectroscopy: A Heterospectral Signal Assignment of Hydrogen-Bonded Complexes. *J. Phys. Chem. Lett.* **2011,** 2, 1106-1110.

39. Keutsch, F. N.; Saykally, R. J., Water clusters: Untangling the mysteries of the liquid, one molecule at a time. *Proc. Natl. Acad. Sci.* **2001,** 98, 10533-10540.

40. Mizuse, K., *Spectroscopic Investigations of Hydrogen Bond Network Structures in Water Clusters*. Springer: Japan, 2013; p 175.

41. Suresh, S., Graded materials for resistance to contact deformation and damage. *Science* **2001,** 292, 2447-51.

42. Fraxedas, J.; Garcia-Manyes, S.; Gorostiza, P.; Sanz, F., Nanoindentation: Toward the sensing of atomic interactions. *Proc. Natl. Acad. Sci.* **2002,** 99, 5228-5232.

43. Lloyd H. Hihara; Tiwari, A. Corrosion Protection Coatings and Methods of Making the Same. US 8,236,203, 2012.

44. Tiwari, A.; Hihara, L. H., Chapter 10 - Sol-Gel Route for the Development of Smart Green Conversion Coatings for Corrosion Protection of Metal Alloys. In *Intelligent Coatings for Corrosion Control*, Tiwari, A.; Rawlins, J.; Hihara, L. H., Eds. Butterworth-Heinemann: Boston, 2015; pp 363-407.

45. Sheremetyeva, N. A.; Voronina, N. V.; Bystrova, A. V.; Miakushev, V. D.; Buzin, M. I.; Muzafarov, A. M., Fluorine-Containing Organosilicon Polymers of Different Architectures. Synthesis and Properties Study. In *Advances in Silicones and Silicone-Modified Materials*, American Chemical Society: 2010; Vol. 1051, pp 111-134.

46. Steward, O. W.; Pierce, O. R., The Effect of Substituent Fluoroalkyl Groups on the Alkali-catalyzed Hydrolysis of Silanes1. *J. Am. Chem. Soc.* **1959,** 81, 1983-1985.

47. Kim, Y.-H.; Hwang, M. S.; Kim, H. J.; Kim, J. Y.; Lee, Y., Infrared spectroscopy study of low-dielectric-constant fluorine-incorporated and carbon-incorporated silicon oxide films. *J. Appl. Phys.* **2001,** 90, 3367-3370.

48. Tripp, C. P.; Hair, M. L., Direct Observation of the Surface Bonds between Self-Assembled Monolayers of Octadecyltrichlorosilane and Silica Surfaces: A Low-Frequency IR Study at the Solid/Liquid Interface. *Langmuir* **1995,** 11, 1215-1219.

49. Sakai, M., Energy principle of the indentation-induced inelastic surface deformation and hardness of brittle materials. *Acta Metall. Mater.* **1993,** 41, 1751-1758.

50. Vernon, M. F.; Lisy, J. M.; Krajnovich, D. J.; Tramer, A.; Kwok, H.-S.; Shen, Y. R.; Lee, Y. T., Vibrational predissociation spectra and dynamics of small molecular clusters of H2O and HF. *Faraday Discuss. Chem. Soc.* **1982,** 73, 387-397.

51. Assender, H.; Bliznyuk, V.; Porfyrakis, K., How Surface Topography Relates to Materials' Properties. *Science* **2002,** 297, 973-976.

52. Bunker, B. C.; Rieke, P. C.; Tarasevich, B. J.; Campbell, A. A.; Fryxell, G. E.; Graff, G. L.; Song, L.; Liu, J.; Virden, J. W.; McVay, G. L., Ceramic Thin-Film Formation on Functionalized Interfaces Through Biomimetic Processing. *Science* **1994,** 264, 48-55.

53. Wallace, S.; Hench, L. L., The Processing and Characterization of DCCA Modified Gel-Derived Silica. *MRS Online Proc. Libr.* **1984,** 32.

Figures only

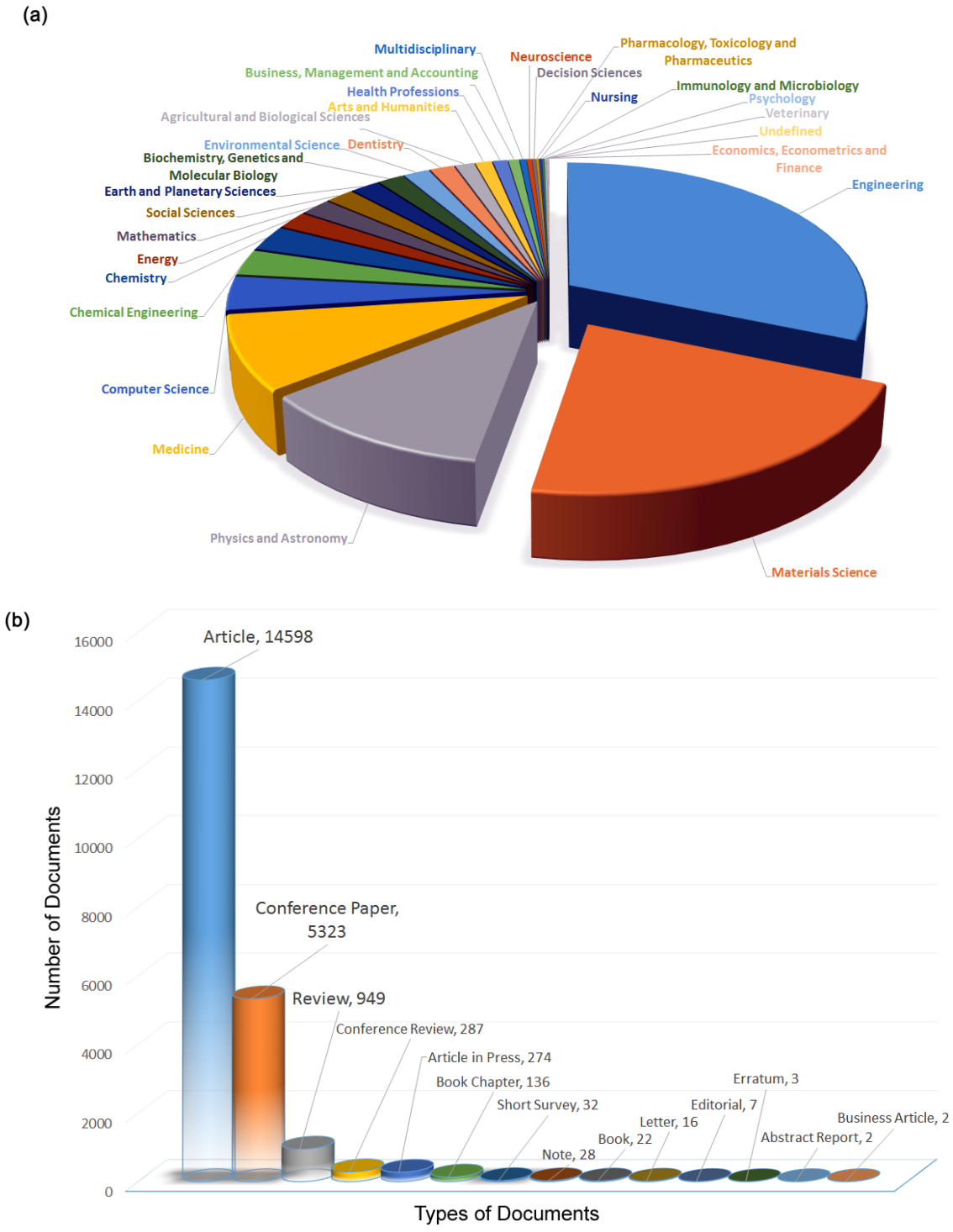

Figure 1: Statistical distribution of articles published in the area of wear analysis in the past 10 years. (a) pie chart showing various areas of science, engineering and technology that discuss wear in materials; (b) bar chart displaying where these articles have appeared.

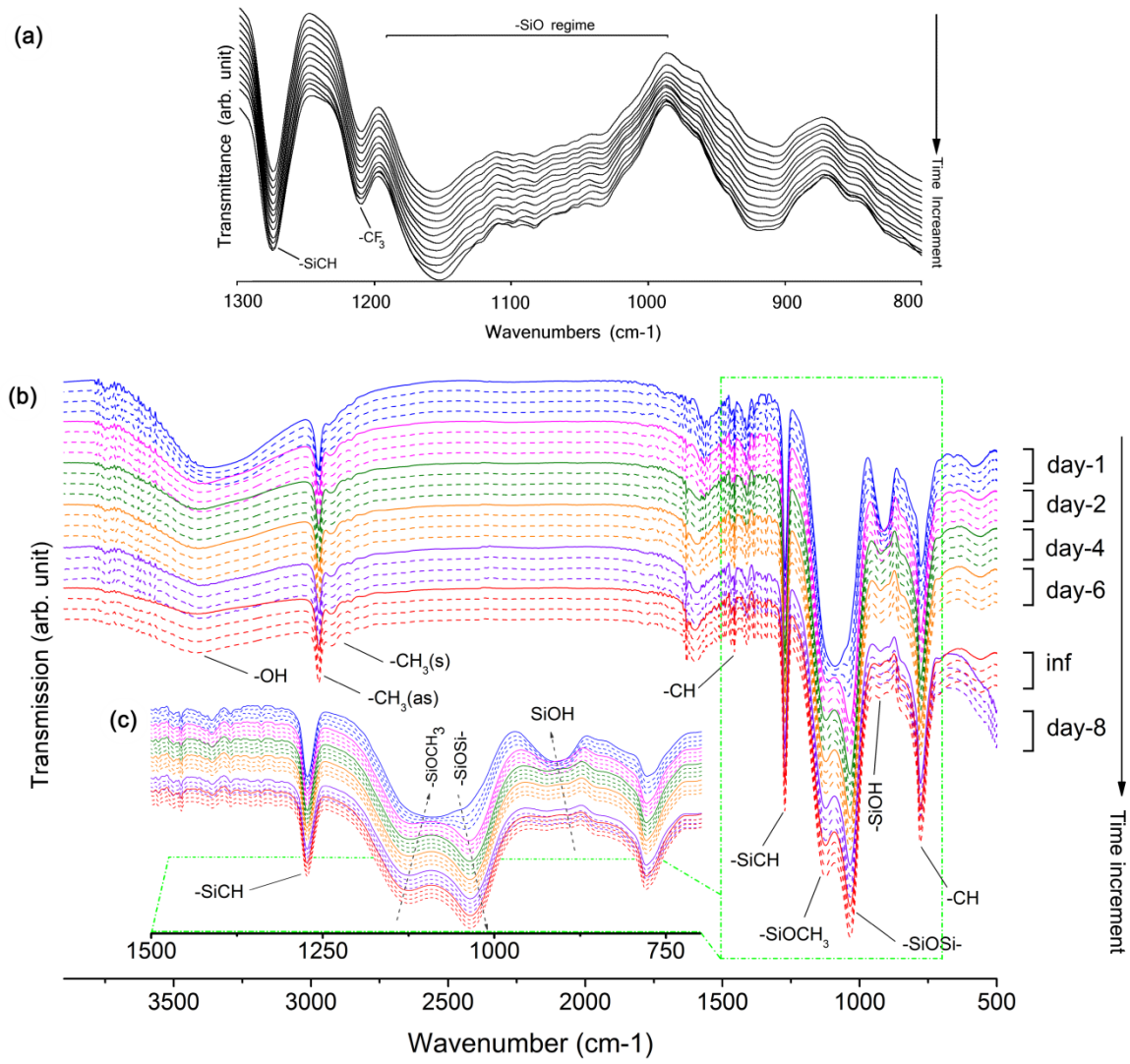

Figure 2: FTIR characterization of PSSQ. (a) Spectra acquired on PSSQ containing 10 wt. % fluorine component; (b) Spectra acquired on PSSQ containing 1 wt. % fluorine component; (c) elaborated region between 750 and 1,500 cm^{-1} showing the changes in band intensities over time.

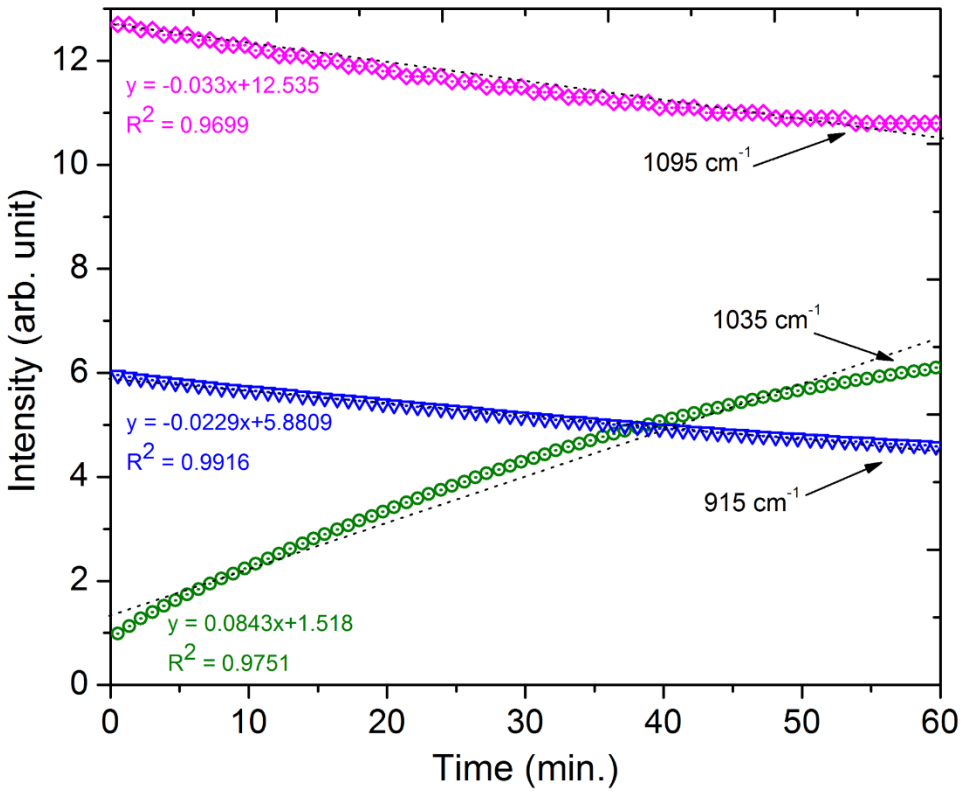

Figure 3: FTIR band intensities during transformation of liquid PSSQ to gel phase. The slope of curves indicates the reactivity of functional groups.

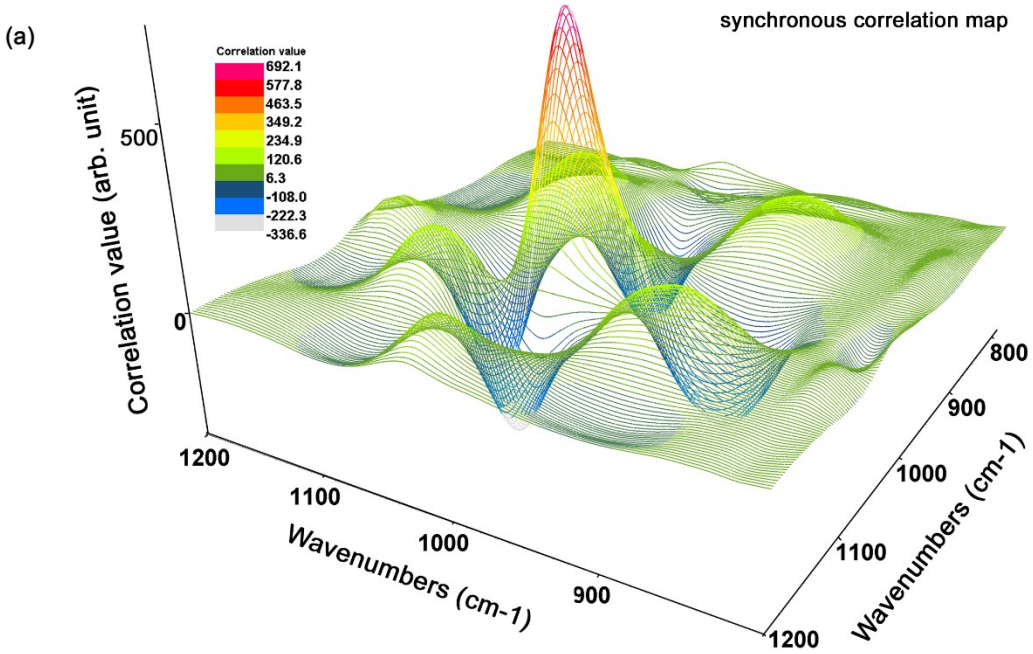

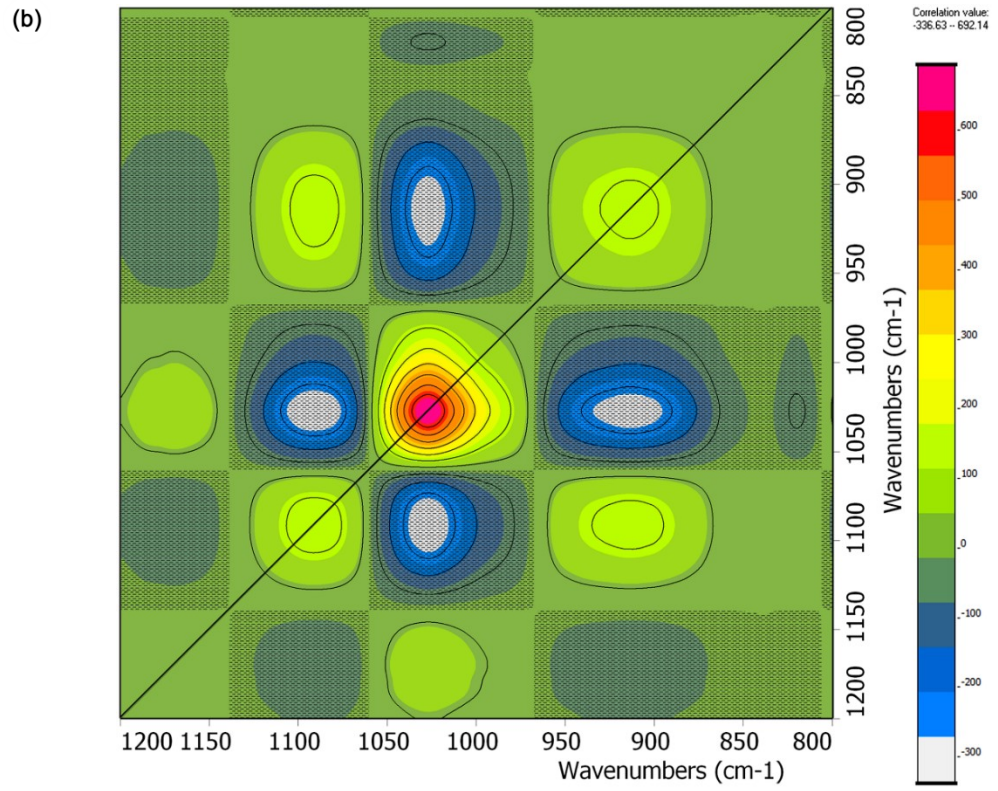

Figure 4: Analysis of hydrolysis and condensation region in PSSQ coating. (a) 3D fishnet plot of synchronous correlation function; (b) 2D synchronous contour map showing auto correlation peaks and cross peaks

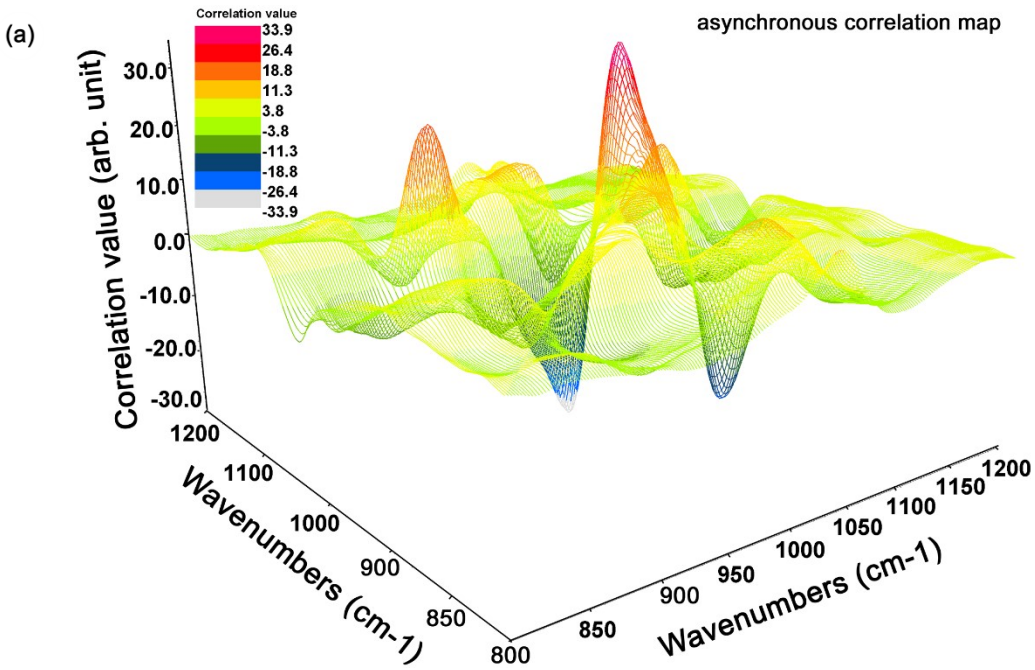

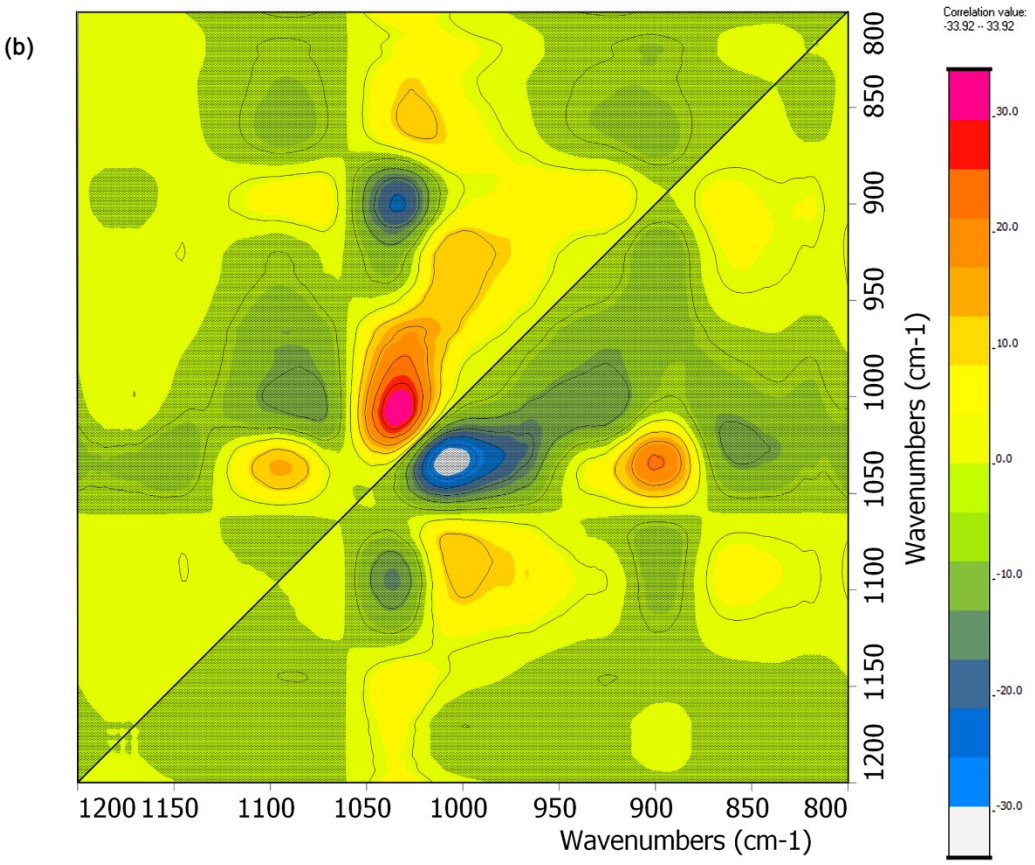

Figure 5: Analysis of hydrolysis and condensation region in PSSQ coating. (a) 3D fishnet plot of asynchronous correlation function; (b) 2D asynchronous contour map showing auto correlation peaks and cross peaks

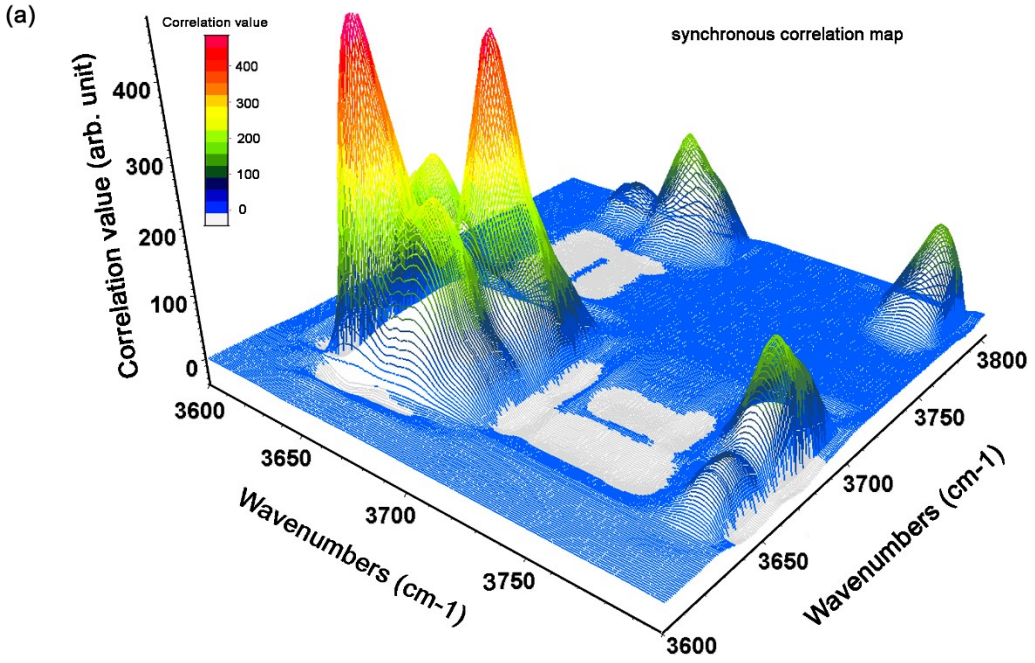

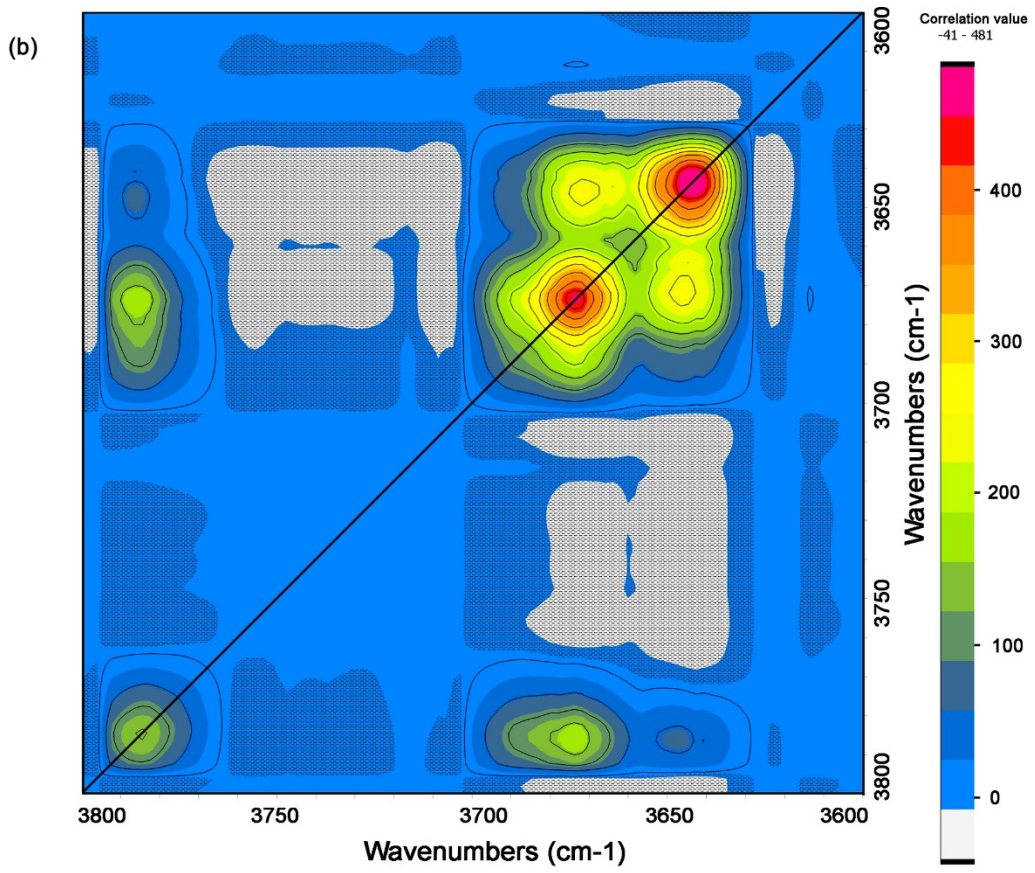

Figure 6: Analysis of hydrogen bonding regime in PSSQ coating. (a) 3D fishnet plot of synchronous correlation function; (b) 2D synchronous contour map showing auto correlation peaks and cross peaks

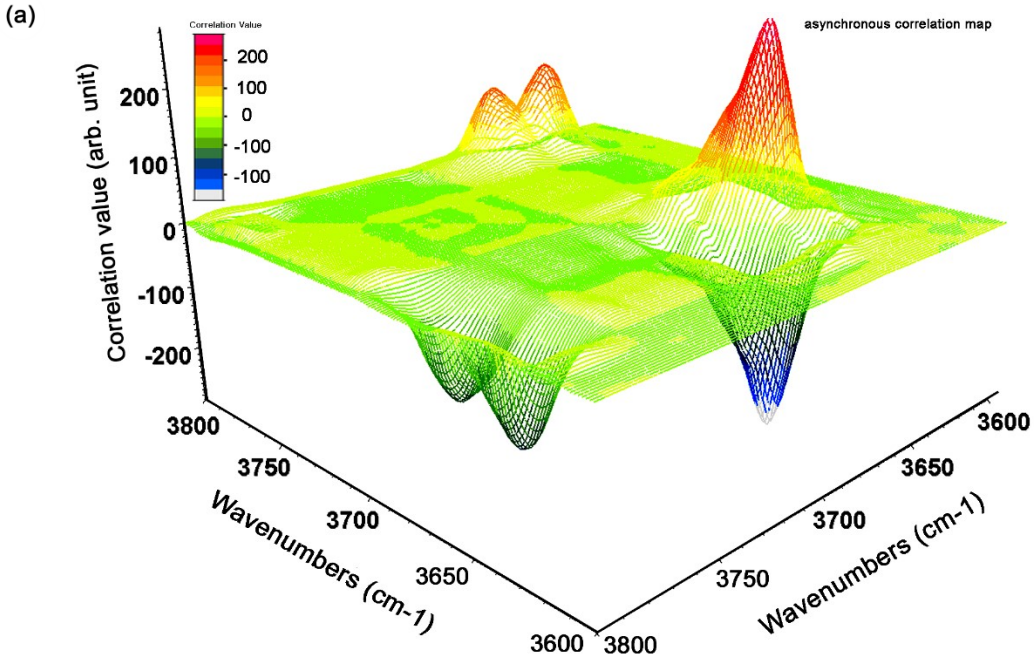

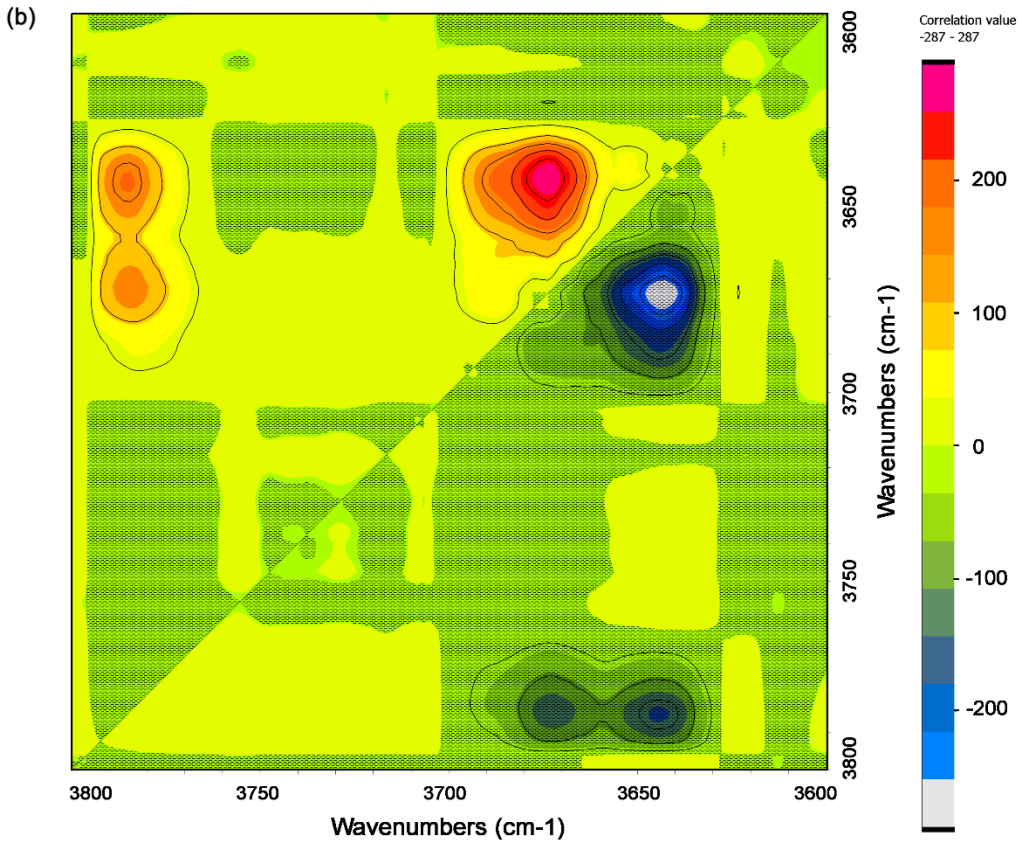

Figure 7: Analysis of hydrogen bonding regime in PSSQ coating. (a) 3D fishnet plot of asynchronous correlation function; (b) 2D asynchronous contour map showing auto correlation peaks and cross peaks

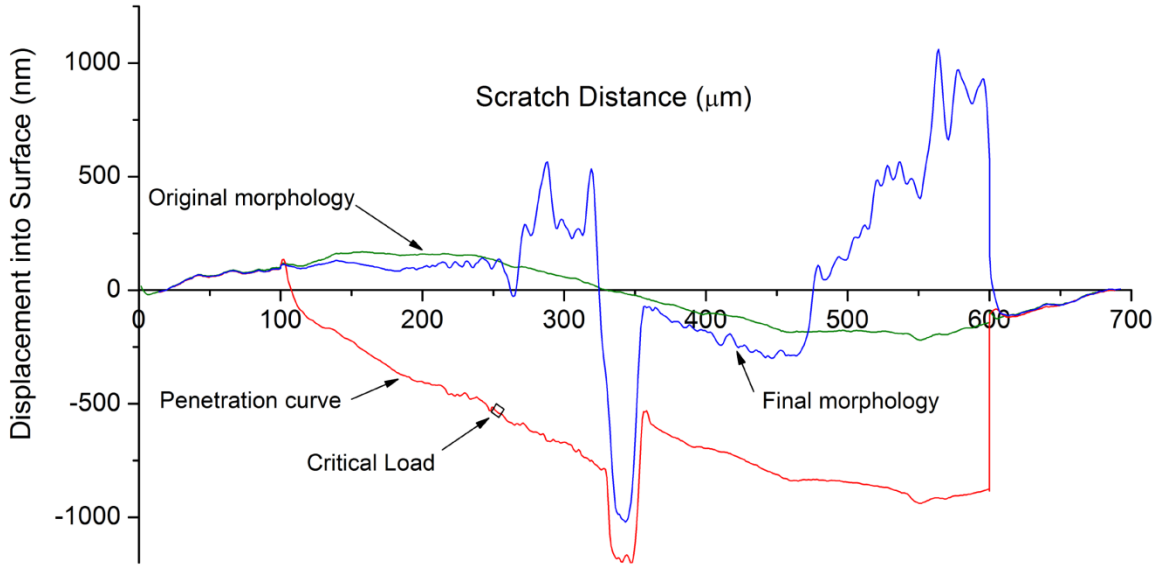

Figure 8: Nanoscratch after 24 h of hardening of $PSSQ_1$. High amount of surface roughness was noticed at this stage, which prohibited the accurate determination of values.

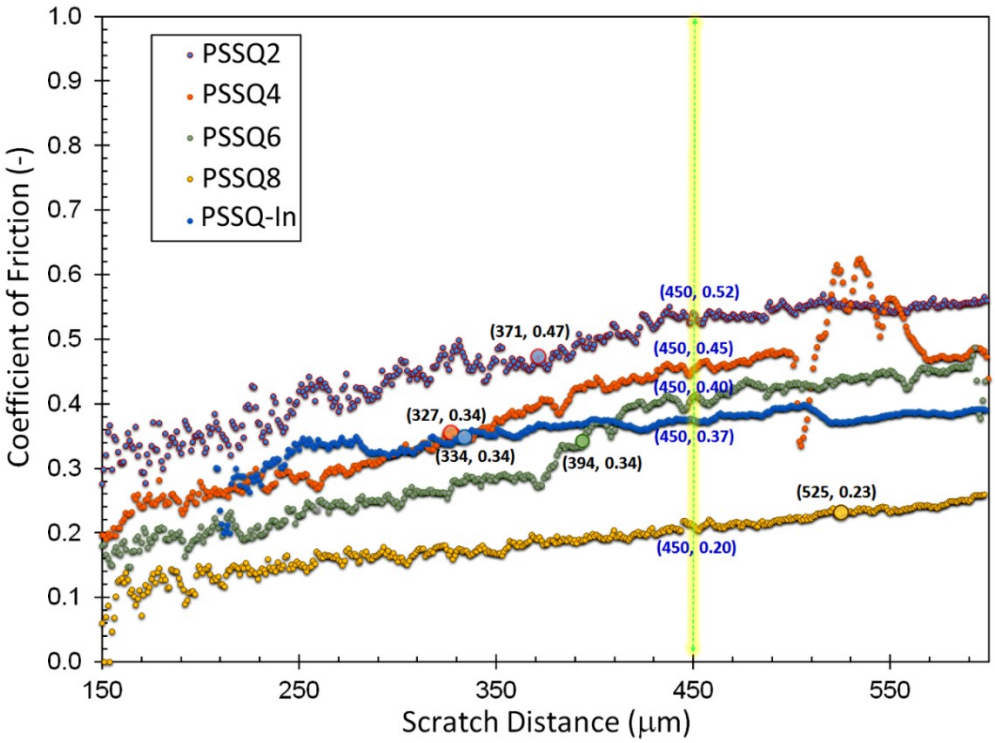

Figure 9: Coefficient of friction values for various curing times plotted as a function of scratch distance derived from nanoscratch testing. Larger bubbles represents the COF values at CL, while the values on the vertical line demonstrate the COF at 450 µm scratch distance for various curing times.

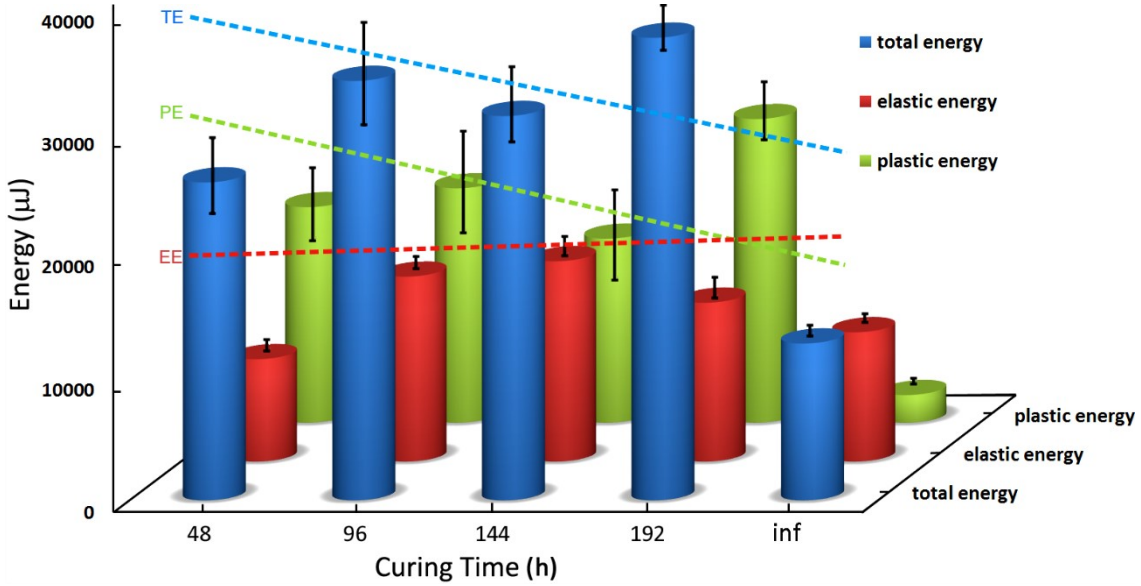

Figure 10: Energy analysis as a function of curing time. The overall trend has been shown through dotted lines for U_{TE}, U_{EE} and U_{PE}.

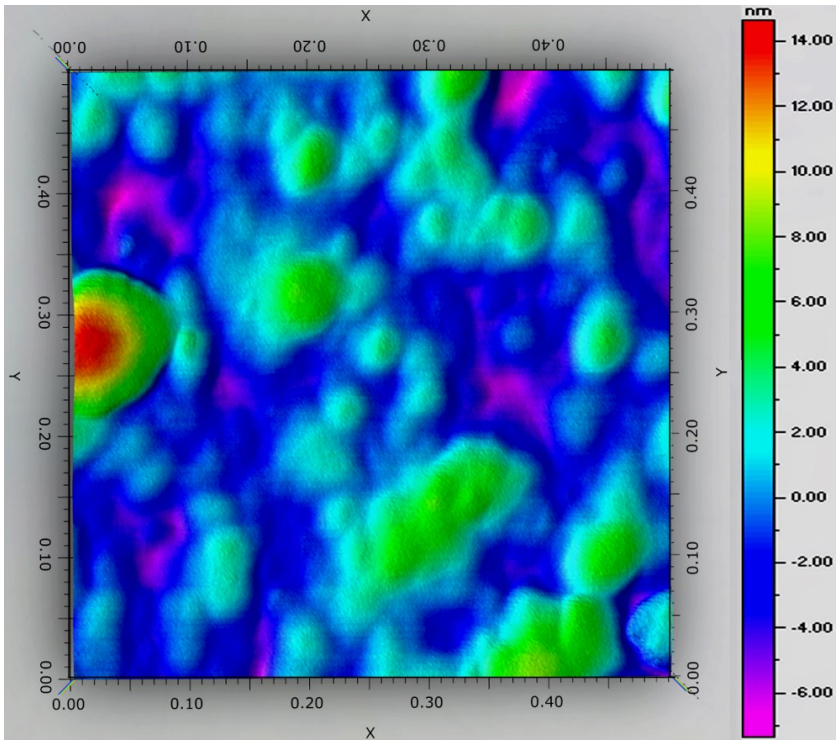

Figure 11: 3D surface topographical scan acquired through AFM after 48 h hardening of $PSSQ_2$. Significant surface roughness was noticed at this stage of hardening, which prohibited the cantilever from acquiring surface topography from a larger area. The scanned area shown here is 500 x 500 nm^2.

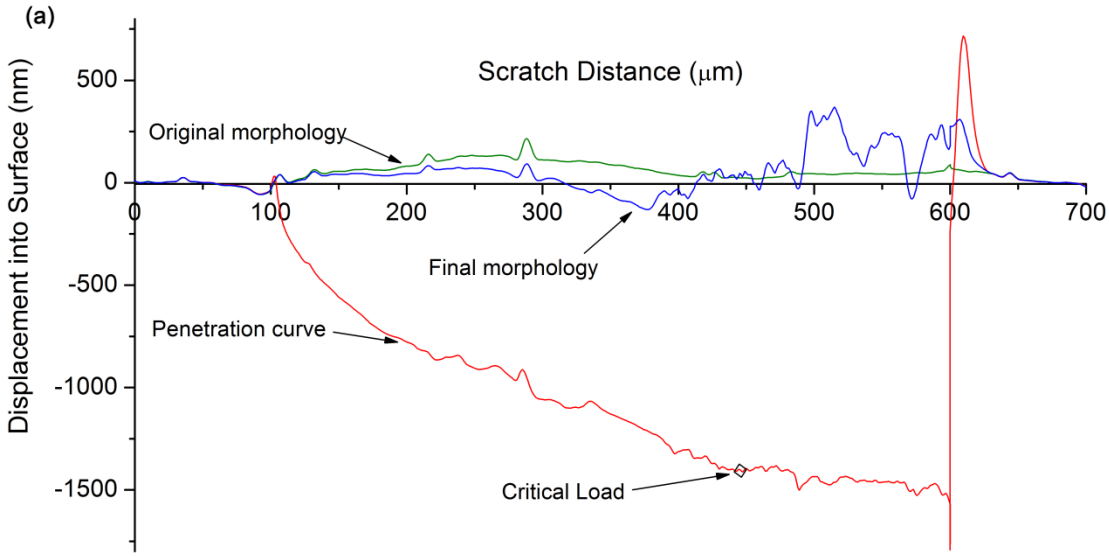

Figure 12a: Nanoscratch test after 48 h hardening of $PSSQ_2$. The coating was relatively hard at this stage and the nanoscratch test recorded an accurate CL value.

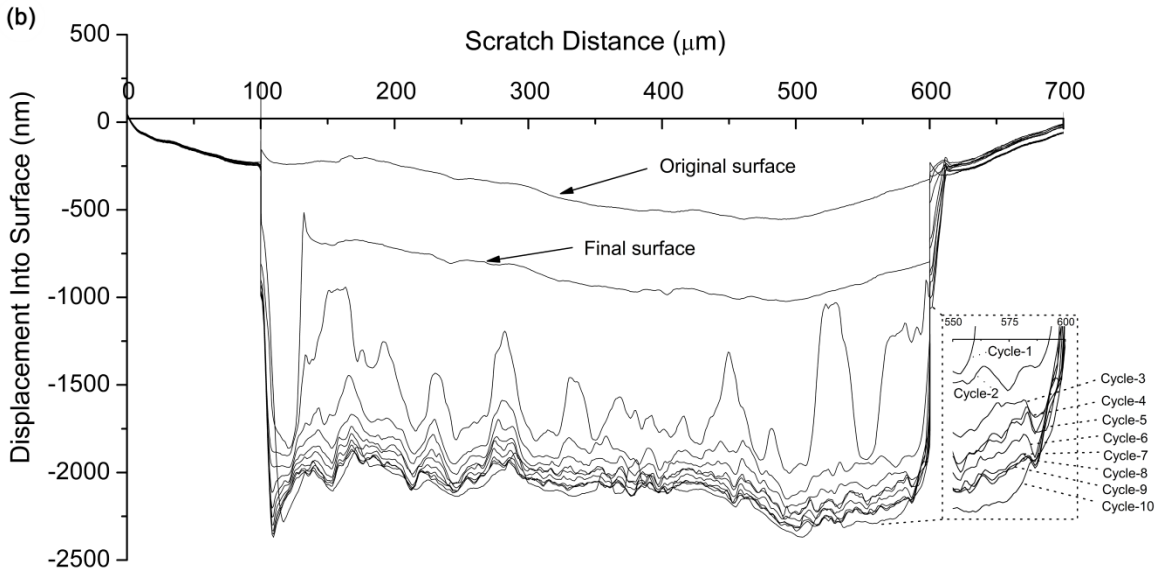

Figure 12b: Wear after 48 h hardening of $PSSQ_2$. In the wear test, the coating was unable to perform well due to incomplete crosslinking and failed in the first wear cycle.

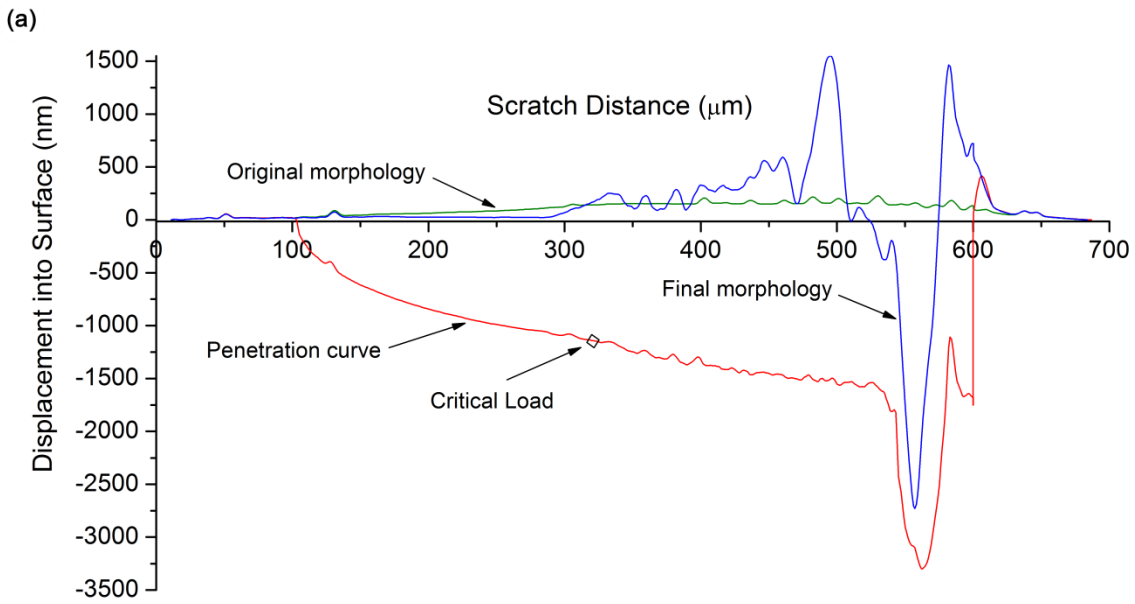

Figure 13a: Nanoscratch test after 96 h hardening of $PSSQ_4$. Relatively little roughness was observed in the original surface scan.

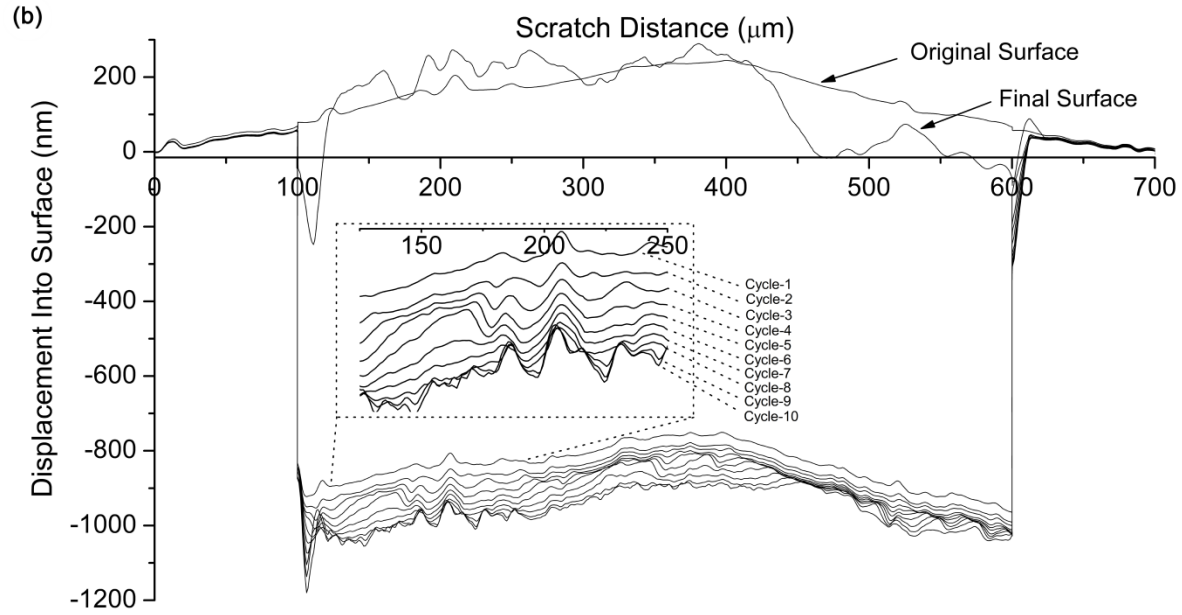

Figure 13b: Wear after 96 h hardening of $PSSQ_4$. The surface hardened at this stage and much less wear was observed in the initial cycles.

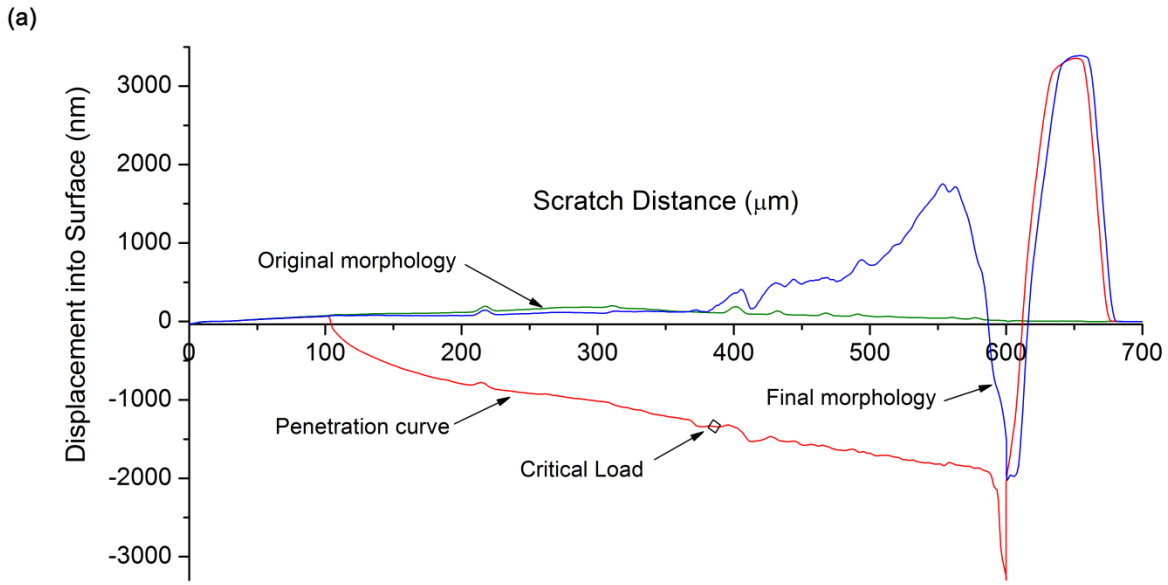

Figure 14a: Nanoscratch test after 144 h hardening of $PSSQ_6$. The increased crosslinking resulted in a higher CL value at this stage.

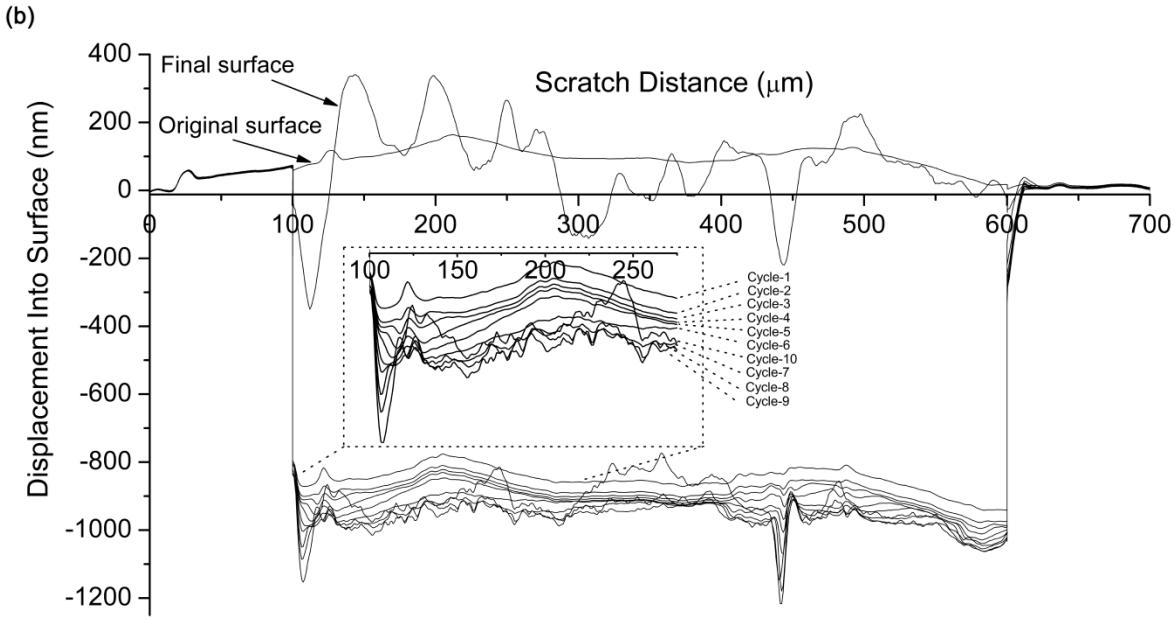

Figure 14b: Wear after 144 h hardening of $PSSQ_6$. The surface contained an extensively crosslinked three-dimensional network, which showed significantly high wear resistance.

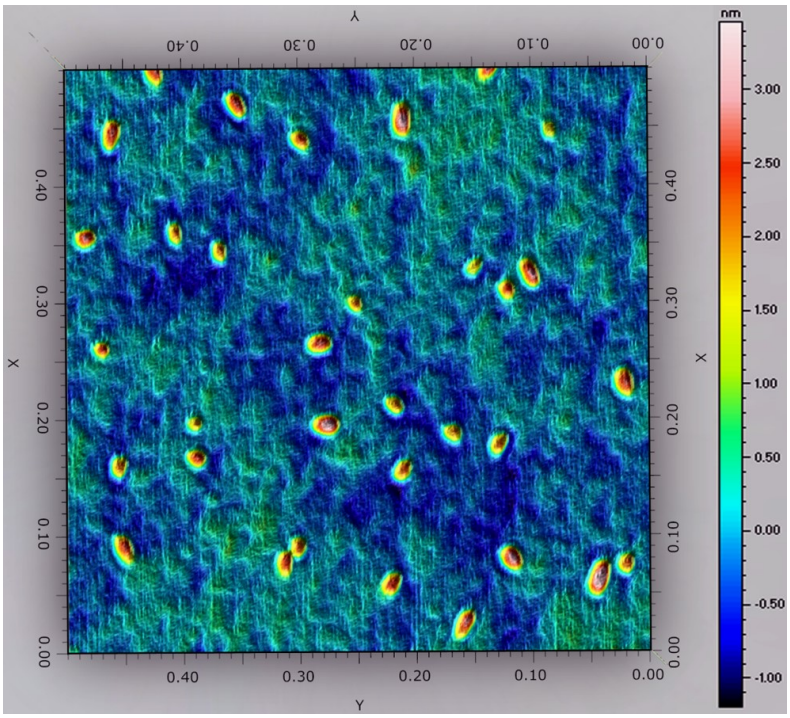

Figure 15: 3D surface topography acquired using AFM after 192 h hardening of $PSSQ_8$. The surface feature at this stage includes the backbone structure, phase-separated islands and distributed nanoparticulates. The scanned area shown here is 500 x 500 nm^2.

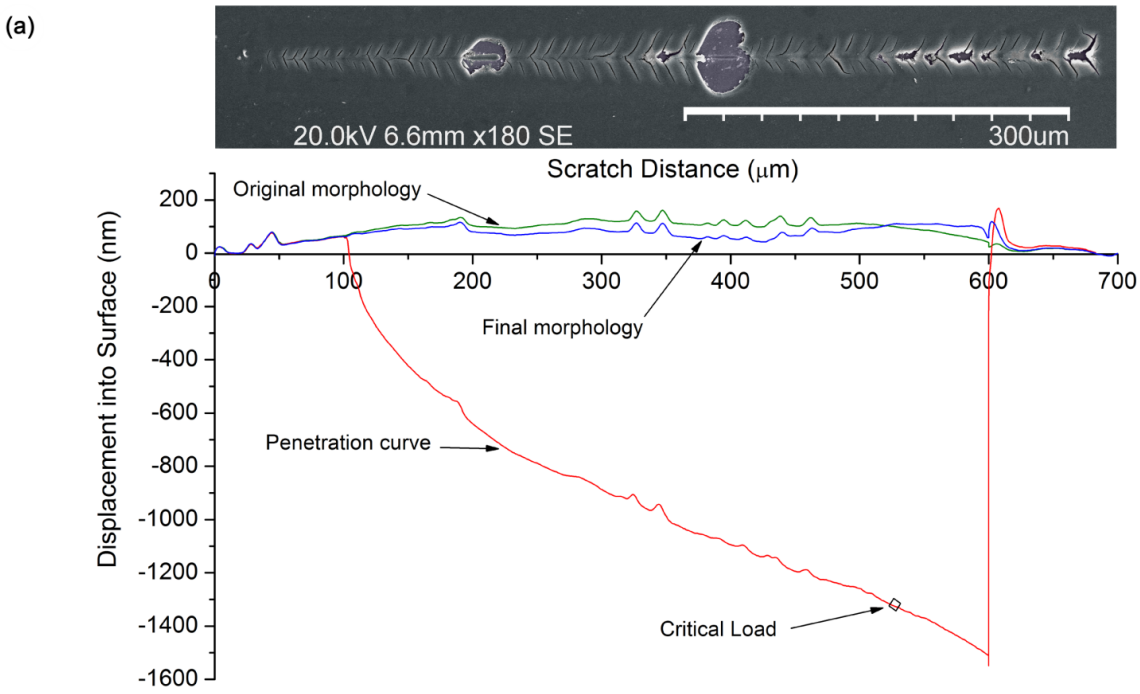

Figure 16a: Nanoscratch test after 192 h hardening of $PSSQ_8$. The SEM image shows various stages of chipping, cracking and delamination in the coating, along with piercing of the metal surface.

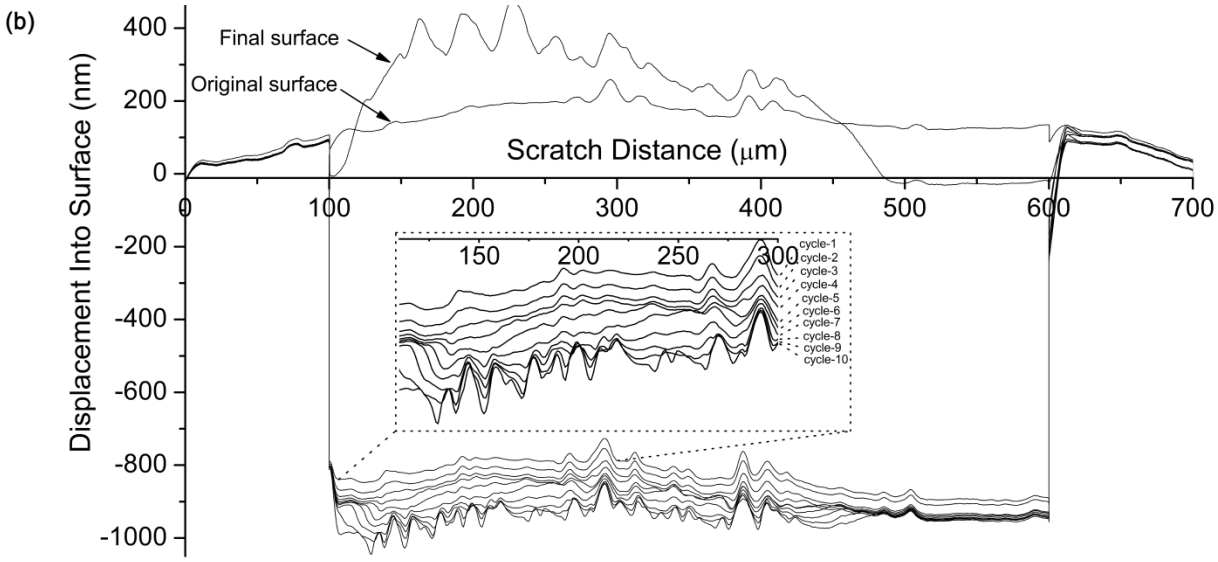

Figure 16b: Wear analysis after 192 h hardening of $PSSQ_8$. The coating reached an ultimate hardening stage and the surface showed exceptionally high wear resistance.

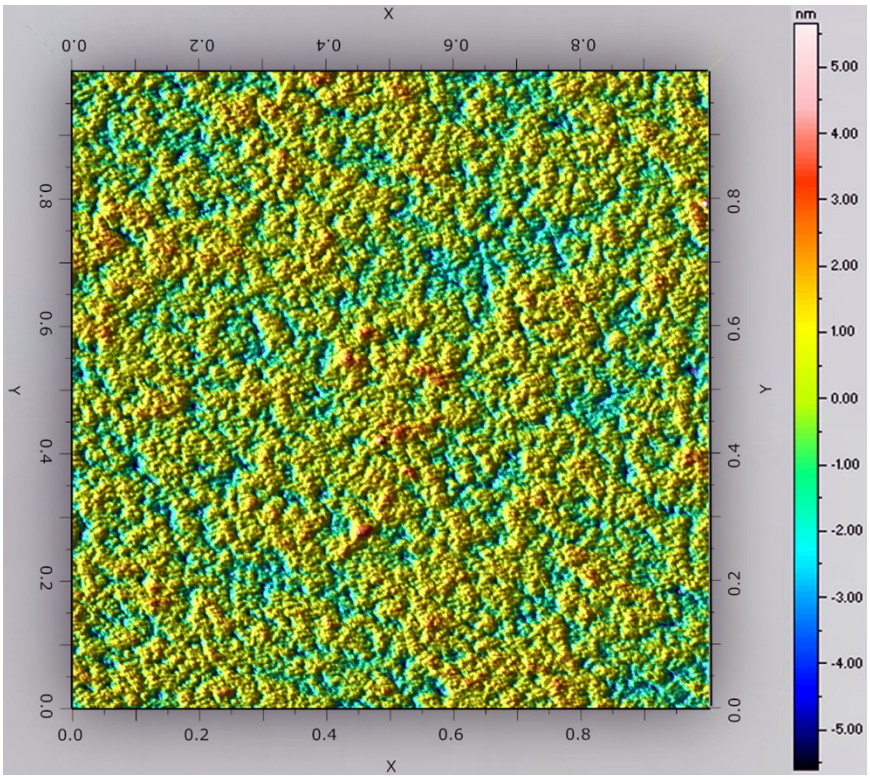

Figure 17: Surface topography after significantly lengthy hardening of $PSSQ_{in}$. The scanned area shown here is 1,000 x 1,000 nm^2.

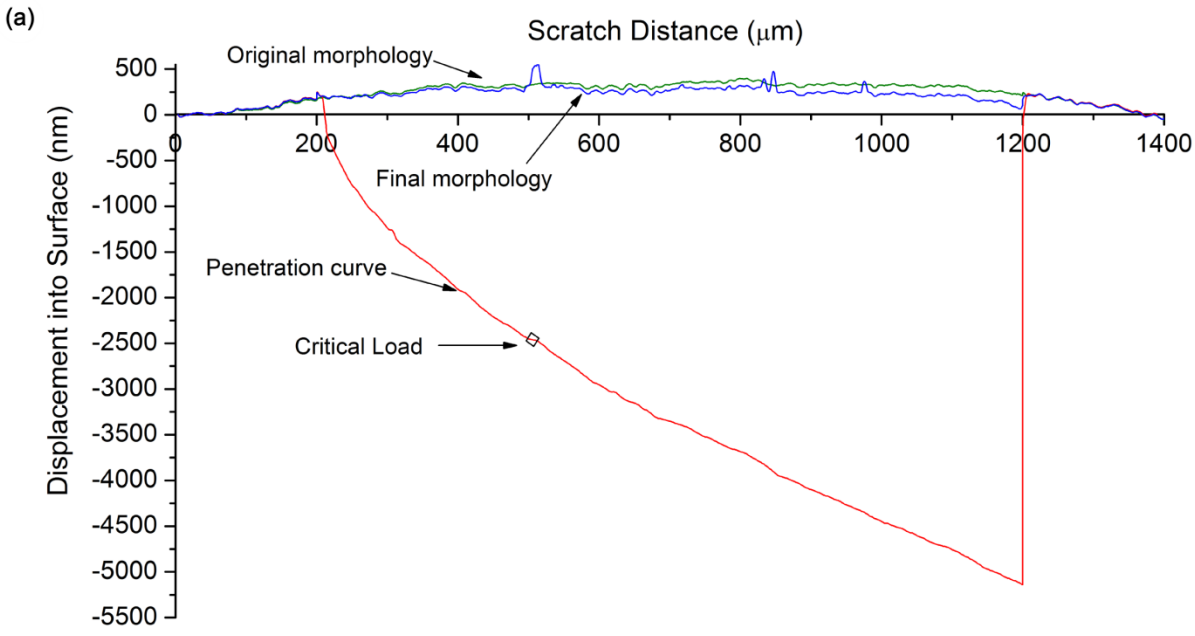

Figure 18a: Nanoscratch test on solid block after prolonged curing of $PSSQ_{in}$. The original and final surface morphology were similar. The cracks occurring during the test helped in determining the CL.

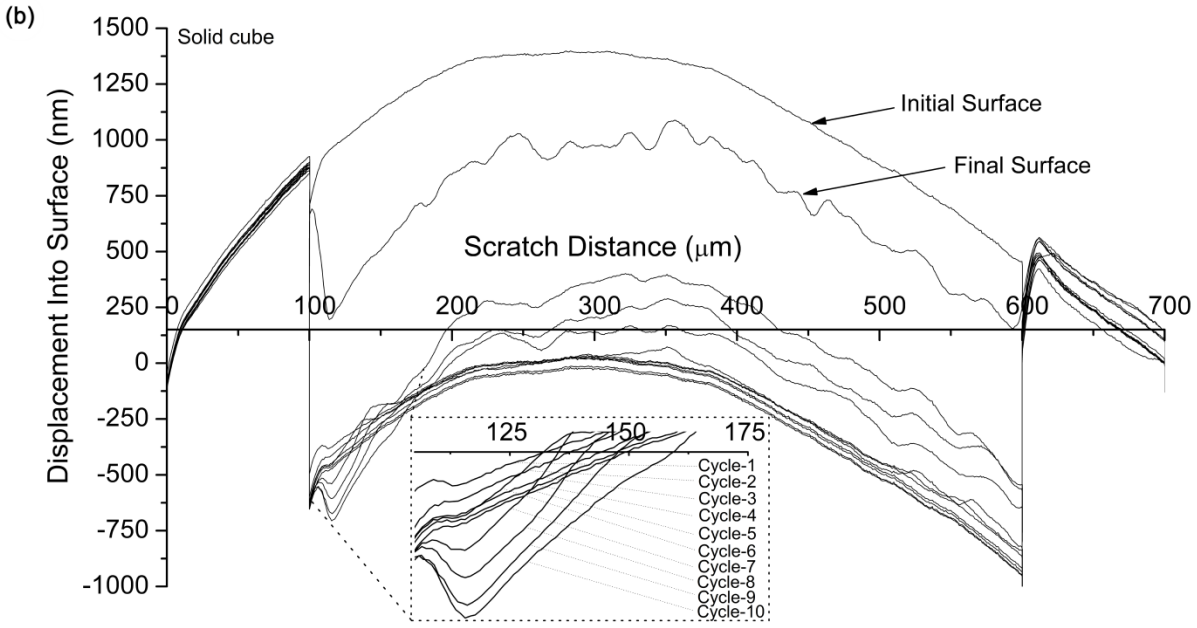

Figure 18b: Wear on solid block obtained after prolonged curing of $PSSQ_{in}$. Unlike other samples, the surface of this sample was not flat. In order to extract true value, the wear test was performed on the pristine surface without any modification.

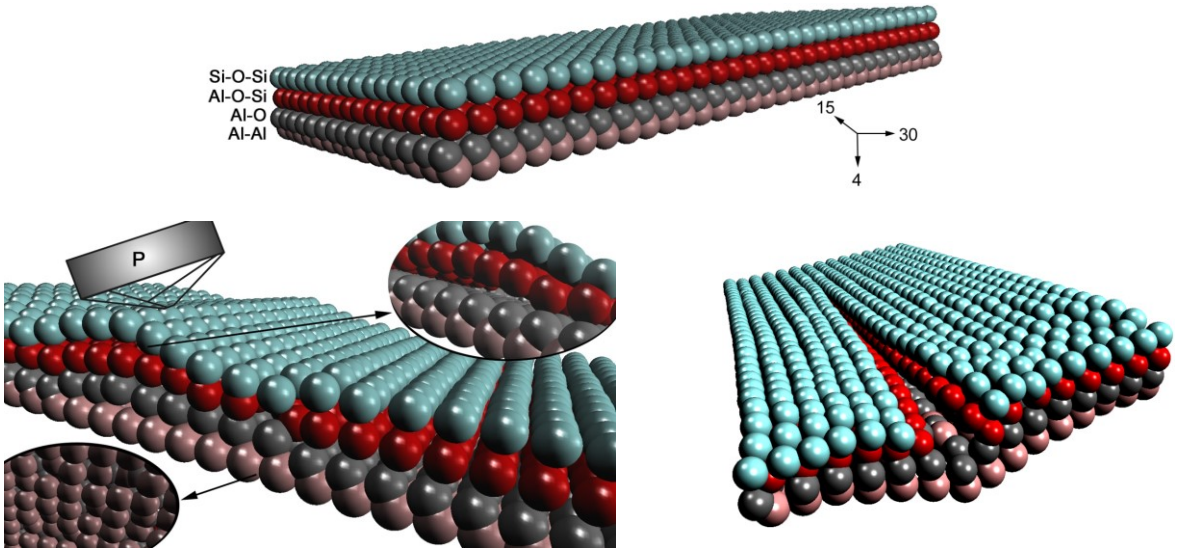

Figure 19: Molecular model representation of PSSQ on aluminium and scratching of surface. The presence of internal residual stresses may result in chipping or delamination of the coating on application of external load.

(a)

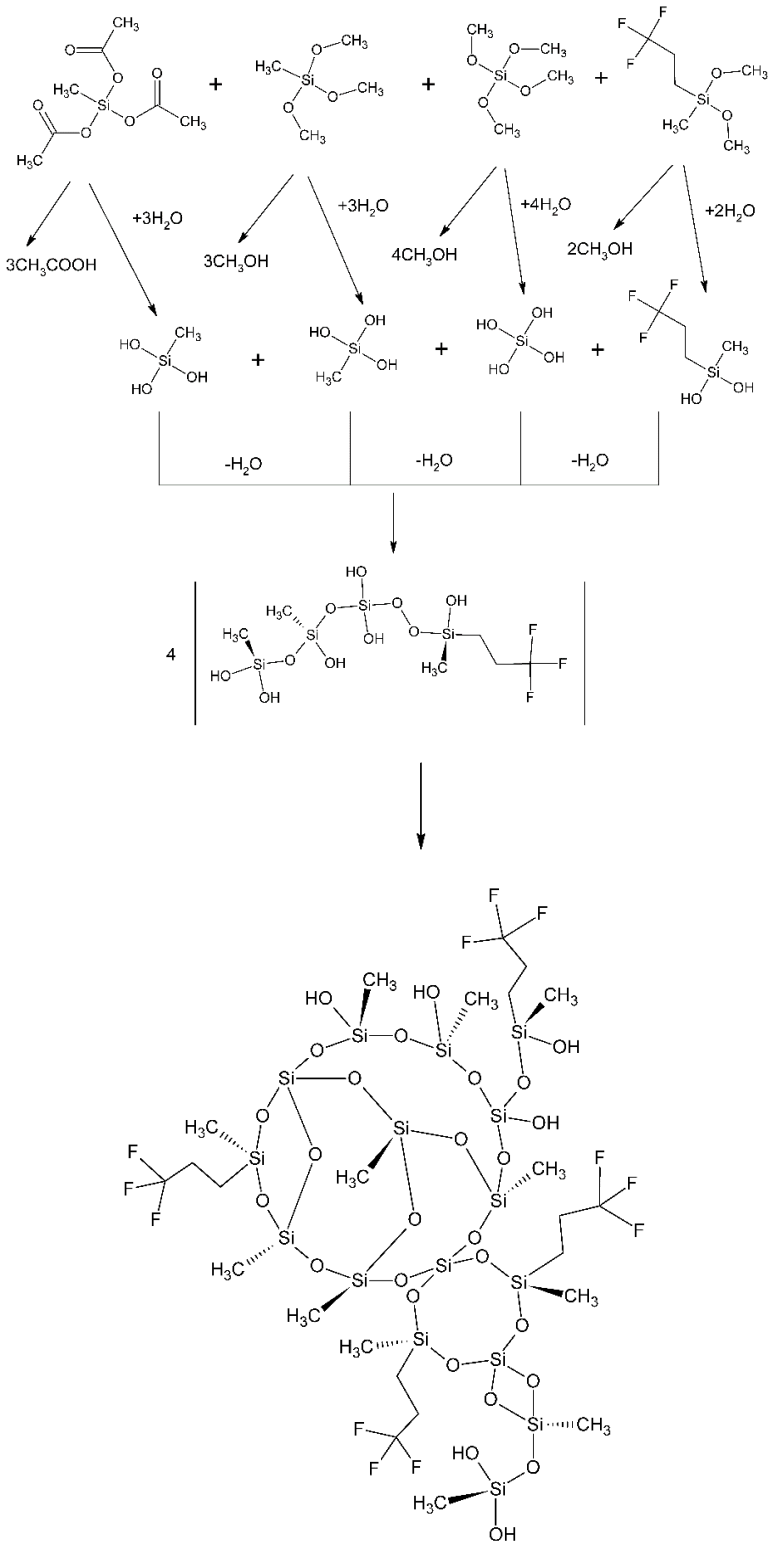

Scheme 1a: Schematic of the hydrolysis and condensation reaction in PSSQ. On addition of a fluorinated compound, phase-separated domains are formed that are scattered in a continuous network.

(b)

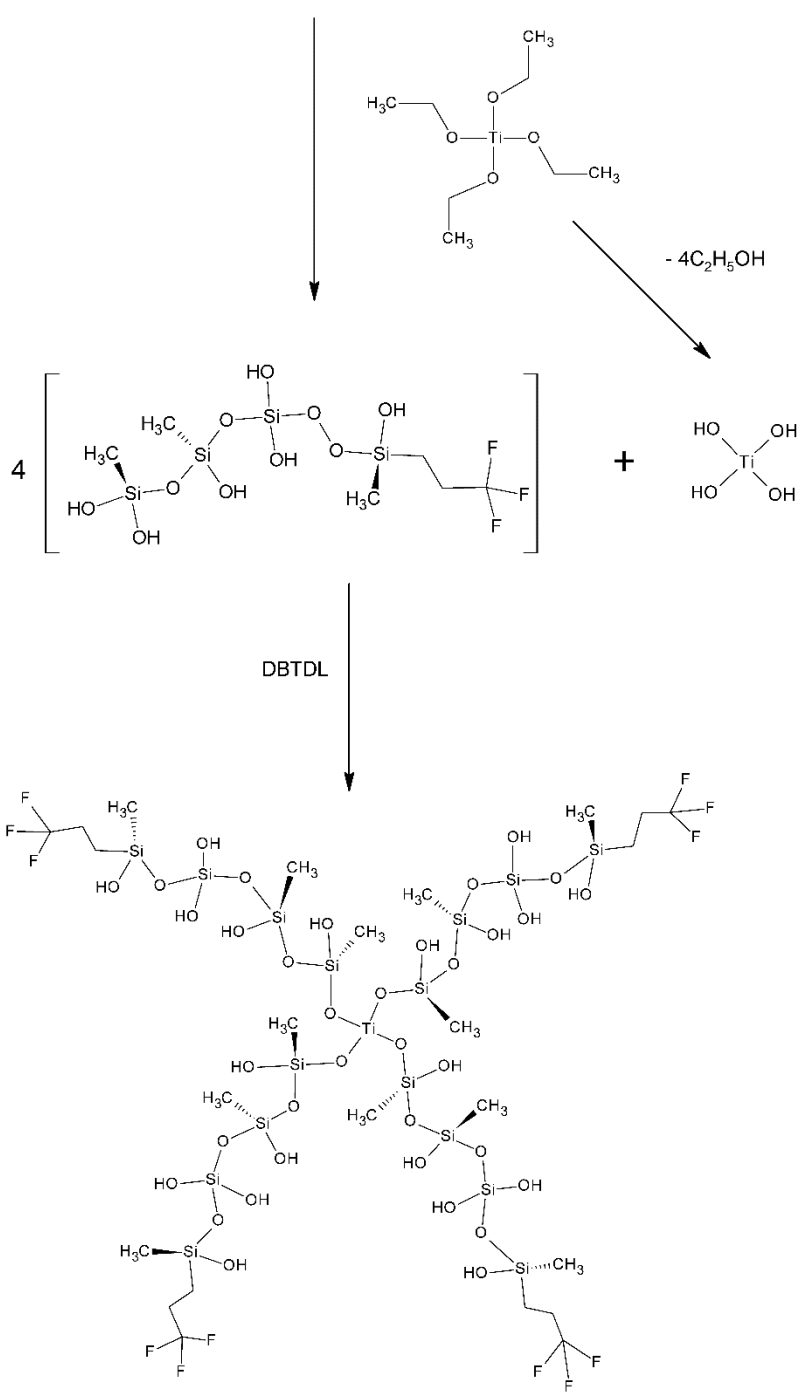

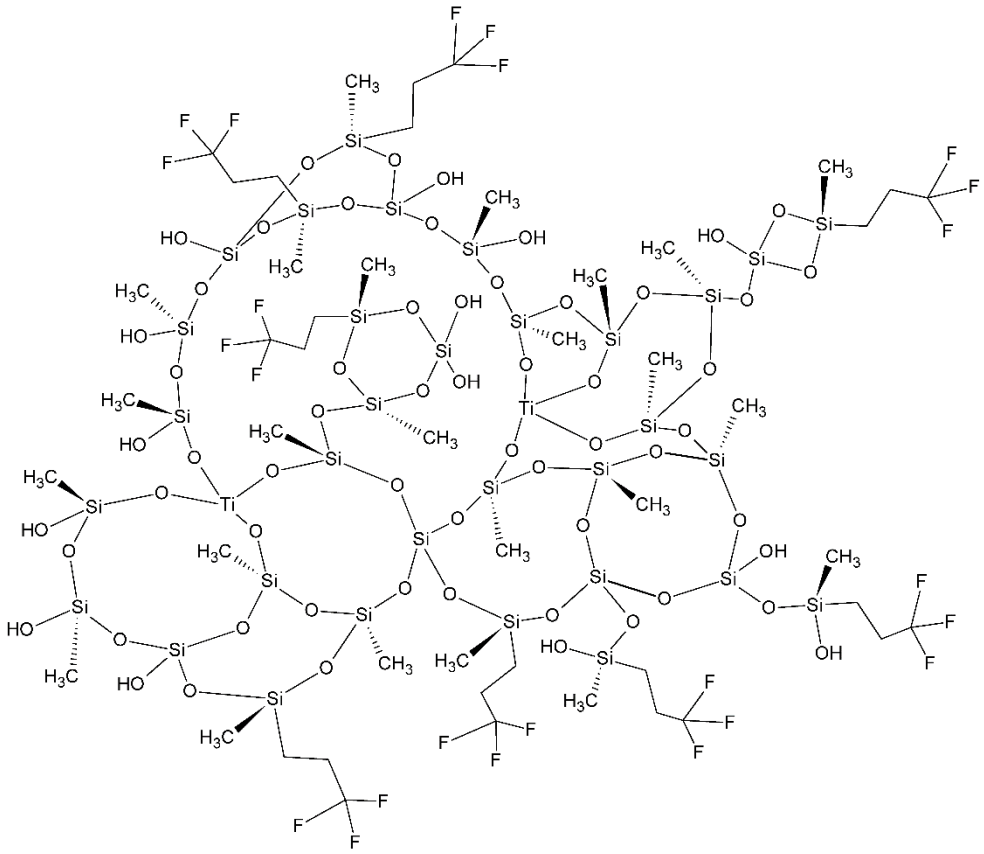

Scheme 1b: Schematic of quasi-dendrimer formation after the hydrolysis and subsequent condensation reaction in PSSQ.

For Table of Contents Only